B. COOLER EXPERIMENT PREPARATION

B.1. Introduction, H.O. Meyer

So far, thirteen research proposals involving the Cooler have been accepted by the IUCF Program Advisory Committee and a total of 265 eight-hour shifts of Cooler beam time have been allocated. Six proposals have been submitted by outside users. For eight of the experiments, active preparations (beam studies, hardware development, and detector tests) have begun.

The potential usefulness and versatility of storage rings is reflected by the wide range of physics questions that are to be addressed by the accepted experiments. In accordance with the overall research interest at IUCF, most of the experiments are in nuclear physics, however, the new experimental environment lends itself to studies in accelerator physics and atomic physics as well, and these topics have a natural place in our program.

The nucleon-nucleon system is the subject of four proposed experiments. The inelasticity in the NN force will be studied using pion production (CE01: Measurements Near Threshold of Nucleon and Few-Nucleon Pion Production, R.E. Pollock and A. Ross, Indiana University; CE03: Kinematically Complete Measurements of $pp \rightarrow pn\pi^+$ Near Threshold, W.W. Daehnick, University of Pittsburgh). A measurement of Coulomb-nuclear interference (CE08: Proton-Proton Analyzing Power in the Coulomb-Nuclear Interference Region, W.K. Pitts, University of Wisconsin) is expected to yield new constraints on NN phase shifts. Finally, a search for narrow dibaryon states in the mass range from 1930 to 2050 MeV/c^2 will be carried out (CE13: A Search for Narrow Dibaryon Resonances with ^{1}H(^{3}He,pp)X, P.V. Pancella and H.O. Meyer, Indiana University).

Proposals to investigate the nucleon-nucleus interaction include the study of the contribution of excited nucleons (CE04: Study of the ^{6}Li(p,Δ^{++})^{6}He Reaction between 400 and 500 MeV, P.P. Singh, Indiana University) and cross section measurements (CE06: Measurements of Nuclear Reactions using Recoil Detection, R.E. Segel, Northwestern University). The determination of the real and the imaginary parts of the forward scattering amplitude through Coulomb-nuclear interference will be attempted (CE07: Forward-Angle Scattering: ^{40}Ar(p,p)^{40}Ar, J. Goodwin, Indiana University). The pion-nucleus potential is the subject of a high-resolution elastic scattering study (CE02: Pionic Atoms as Compound States in Nucleon-Nucleus Collisions, H.O. Meyer, Indiana University). Using Coulomb breakup of polarized deuterons in the field of a heavy nucleus is a method of producing a polarized, secondary neutron beam (CE10: Preliminary Tests for a Tagged, High-Resolution, Polarized Neutron Beam, J. Cameron, Indiana University).

The Indiana Cooler program also includes studies at the forefront of accelerator physics. One such measurement (CE05: Experimental Test of the Siberian Snake Concept, A.D. Krisch, University of Michigan) is to deliver the experimental proof of a scheme to eliminate depolarizing resonances by introducing spin- precessing longitudinal magnetic fields (see Krisch el al. in the research section of this report). Another topic of current interest concerns ordering and collective phenomena in stored, cooled beams (CE12: Search for Ordering in Cold Ion Beams, J.P. Schiffer, University of Chicago).

Since the Cooler environment seems to be especially suited to such measurements,

two atomic physics experiments are part of the current research program. A study of the process in which an atomic system captures an electron while simultaneously being excited, followed by de-excitation by photon emission uses the cooling electrons as the target (CE11: Measurement of Dielectronic Recombination, J.A. Tanis, Western Michigan University). Another atomic physics experiment (CE09: Measurements of Electron Capture Cross Sections, A. Ross, Indiana University) aims to measure cross sections for electron pick-up by medium-energy protons when passing through a target.

The diversity of the proposed experiments is mirrored by the range of experimental conditions that are required. Most of the experiments on the list call for proton beams. The majority of these eventually will need polarized protons. Polarized deuterons and beams of singly- and doubly-charged ^{3}He ions are also requested. Half of the experiments will make use of the extension of the cyclotron energy range that is offered by the Cooler. Internal gas targets of H, He, N, Ar, Kr, and Xe are requested and for some measurements polarized H and D targets from an atomic beam source will be used eventually. In three cases solid C targets and in one case a Li target is required.

The first nuclear physics experiment to be attempted (CE01) requires the detection of coincident protons inside a forward cone of up to 20° half angle with good energy and angular resolution. The corresponding setup, mounted in the G section, has been completed. It consists of a multi-purpose target box whose downstream end is a thin window to which the continuing beam pipe is joined by brazing. This window is followed by a sequence of scintillator and wire chamber detector planes, schematically shown in Fig. B1. The scintillators are segmented to obtain a fast multiplicity signal. The detectors

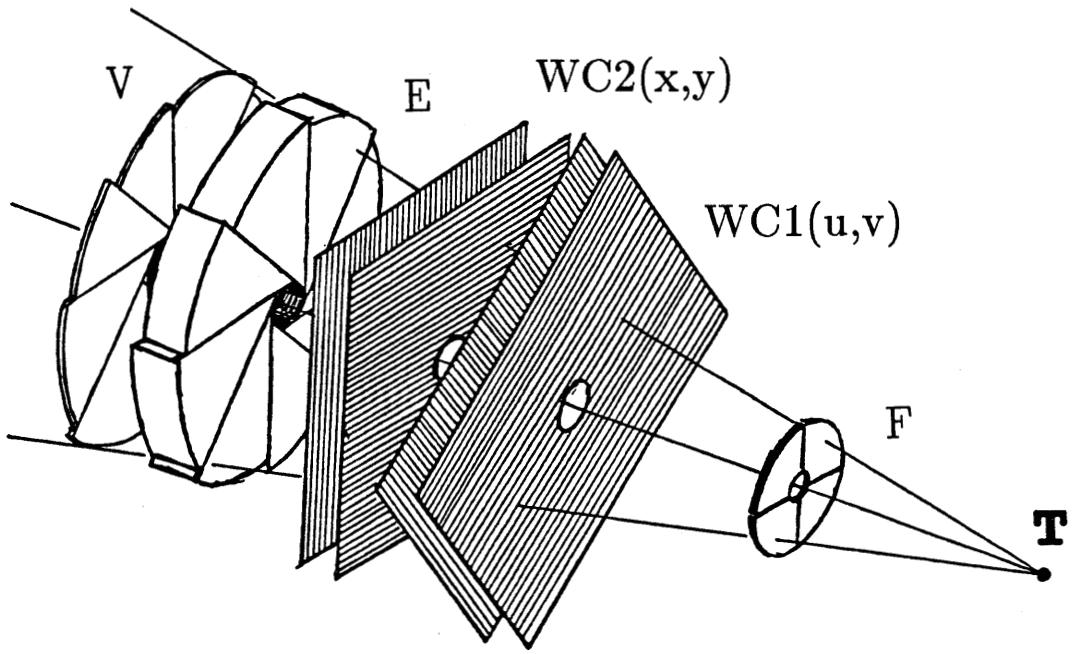

Figure B1. Perspective view of CE01 detectors, active volumes only, not to scale. F, E, and V are the front, total energy, and veto scintillators, respectively, WC1(u,v) and WC2(x,y) are the two identical wire chambers used for tracking, and T is the target location. All five units can be moved independently along the beam axis.

almost completely cover a forward cone whose opening angle is determined by the (variable) position of the detector planes along the beam. The Cooler beam pipe continues through the center of the stack, causing a 1°-2° wide dead region. The requirement to make the central dead region as small as possible, has led to a unique wire chamber design with a central opening structure that is supported solely by the thin foil planes and the sense wires. The chambers feature single-wire readout and have been designed to resolve ambiguities associated with multiple prongs; they are also used for particle tracking, which is valuable during the commissioning of the experimental setup. Event processing makes use of remote-controlled ECL CAMAC modules, connected to a dedicated MicroVAX.

In the year covered by this report, considerable progress has been made in Cooler development, in making detectors and the acquisition system ready for the first experiments, and in gaining experience with a variety of internal targets. A group of about ten staff physicists, post-docs and students are studying topics that are connected with the use of the Cooler as a research tool, with the goal to prove the feasibility of a first experiment. This activity is in preparation for regular scheduling of runs for the, as of now, thirteen approved Cooler experiments.

B.2. Target Development

A. Berdoz, J. Doskow, W. Lozowski, H.O. Meyer, P. Pancella, T. Rinckel, H. Rohdjess, A. Ross and F. Sperisen.

B.2.1. Gas Jet

Supersonic gas jets employ known technology and are operated routinely at high-energy storage rings at target thicknesses of a few times 10^{14} nuclei per cm^2. Buffer cells, where a high-pressure region is separated from the good ring vacuum by a differential pumping arrangement have been suggested as an alternative scheme. The latter is especially interesting when the cell is filled from a polarized atomic beam source. The gas target which has been built at IUCF for use in the Cooler[1] is a combination of the two methods. It contains a jet in a region that is separated from the rest of the ring by three stages of differential pumping. Operating the jet nozzle at room temperature, we have achieved target thicknesses of up to 10^{15} cm^{-2} for H, N, or Ar gas. The feeding line is equipped with a fast switching system in order to be able to turn the target on only during the data taking period of the cycle.

Since the differential pumping requires apertures close to the beam, an important design criterion is the minimization of background generated by the transverse tails of the beam distribution interacting with these apertures. At the moment, the gas target has been removed from the target box in order to investigate the effect of aperture-defining slits (under construction) on the tails of the beam distribution in the target region. For these tests solid targets will be used.

B.2.2. Fibers (Micro-Ribbons)

In the past year tests have begun with carbon micro-ribbons in the Cooler, using the CE01 target chamber and detector system. Thanks to the ray-tracing capability of this

system, protons scattered from the target could be cleanly separated from the background. Our tests done so far demonstrate the viability of thin ribbons as internal targets in storage rings. A variety of evaporable materials can thus be made accessible for experiments.

A commercially available carbon fiber of 7 μm diameter corresponds to t = 4.3×10^{16} nuclei per cm. At IUCF we are able to make ribbon-shaped carbon fibers as thin as t = 1×10^{15} cm^{-1}. The method involves electron-beam evaporating graphite or isotopically enriched ^{13}C through a mask onto a substrate (glass slide). The mask consists of parallel, 50 μm diameter tungsten wires with spacings ranging from 15 to 60 μm; it is made on a machine normally used for wire chamber manufacturing. During evaporation, the glass plate rests on the wires. It is covered in advance with a parting agent by wiping over the surface one drop of a solution of betaine monohydrate, sucrose, and water (7:1:28). The evaporated carbon layer has a thickness of 12 μg/cm^2. The resulting strips are floated off in water, picked up at one end with a fine needle, aligned and dried in a gentle air stream and mounted with some slack on both ends on a fork-like target holder, using small drops of a cyanoacrylate bonding agent.

Consider first a fiber or micro-ribbon positioned at the center of the stored beam. Due to their betatron oscillations all beam ions have a chance to hit the target occasionally. Assuming that the beam width w is much larger than the width of the fiber and that the beam profile is uniform, the average target thickness is given by[2]

$$< d >= \frac{4t}{\pi \cdot \mathrm{w}} \quad , \tag{1}$$

where t is the linear density of the fiber (atoms per unit length). Typically, for our micro-ribbons described above, t = 1×10^{15} atoms/cm and w = 1 mm, we get $< d > = 1.3 \times 10^{16}$ atoms/cm^2. For carbon, this thickness is too large because it causes the beam lifetime to become short compared to the typical overhead time of the Cooler run cycle, resulting in a low average luminosity.[3] The target thickness can be reduced by moving the beam back and forth across the fiber (thus effectively increasing w in eq.(1)), or, equivalently, wiggling the fiber across the stationary beam. If this is a harmonic motion with amplitude $x_o >>$w, symmetric about the stationary target (or beam, respectively), the time-averaged thickness becomes

$$< d >= \frac{t}{\pi \cdot x_o} \quad . \tag{2}$$

We have developed a method to wiggle micro-ribbons with an amplitude of about 5 mm, thus achieving an average target thickness 20 times lower than with the stationary ribbon, or roughly 6×10^{14} atoms/cm^2. The setup is shown in Fig. B2. The ribbon target is attached with slack on both ends to a fork-like target holder. The transverse ribbon motion is induced by applying alternating voltage (a few hundred volts, 20-200 Hz) to a nearby electrode. The target holder is mounted on a rotary vacuum feedthrough (not shown), driven by a stepping motor, so the target can be moved into the beam just before data taking starts and kept out during the beam preparation phase. Fig. B3 shows data taken with 108 MeV cooled protons scattered from a wiggling micro-ribbon. Ray-tracing allows for clean separation of target scattering from background. The measured beam lifetime of 0.52 s is considerably shorter than what would be expected on the basis of the

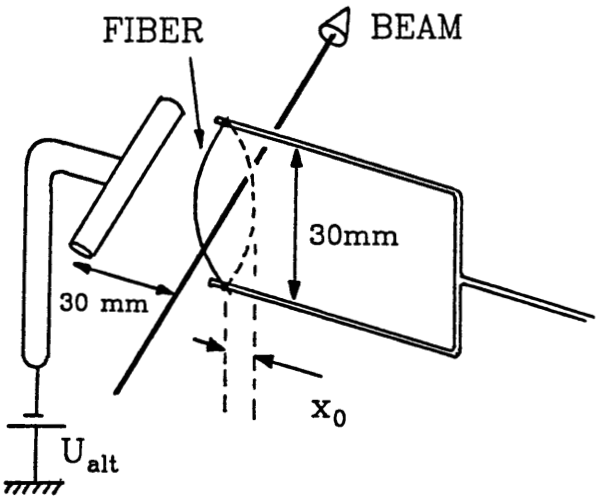

Figure B2. Arrangement for a wiggling micro-ribbon carbon target. The wiggling motion is induced by an alternating electric field, U_{alt}.

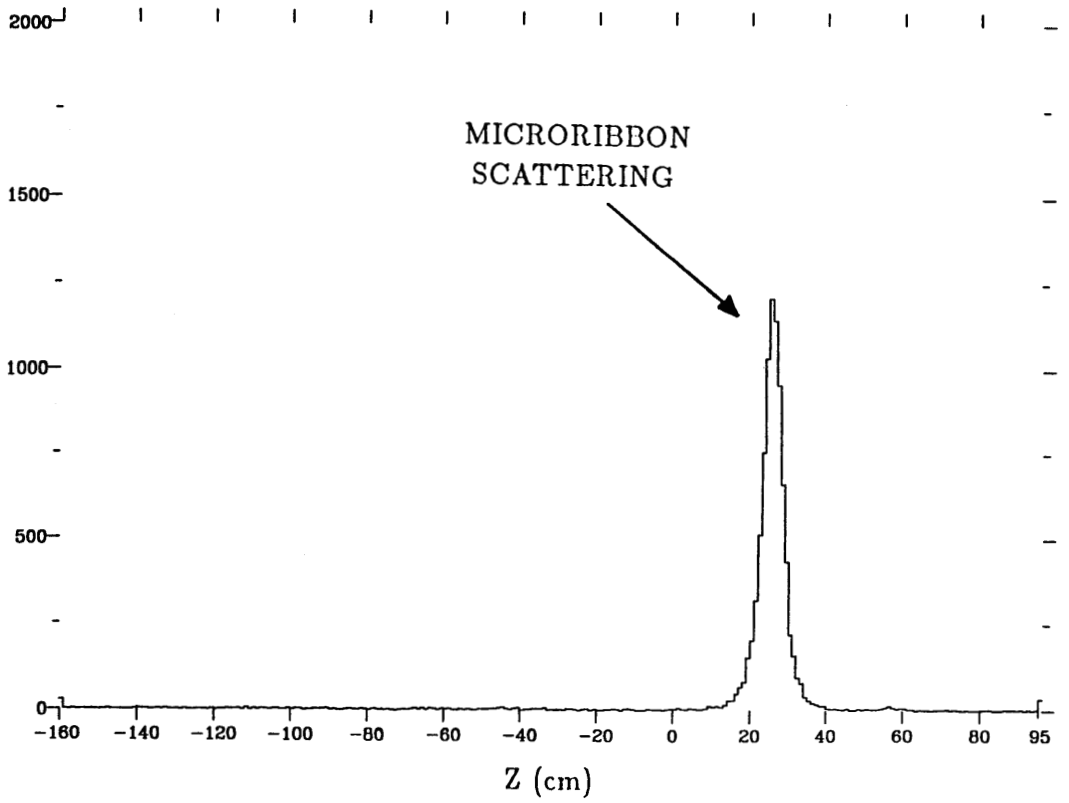

Figure B3. 108 MeV cooled protons scattered from a wiggling carbon micro-ribbon. Plotted is the distribution of the vertices of reconstructed scattering rays along the beam axis.

design parameters of the ring.[3] The scattering cross-section derived from this measurement is within a factor of three of the expected value which is within the present uncertainties in determining the target thickness and the stored beam current.

For some experiments the peak luminosity during the passage of the ribbon through the beam may be too high and cause dead time problems. At our wiggling frequency the time of passage is of the order of 1 ms, comparable to the time it takes to process one event in our data aquisition system. It would thus be desirable to increase this frequency but with the method described above this does not seem to work. To get around this difficulty we have attempted to wiggle the beam instead, while leaving the micro- ribbon stationary. This was done by modulating the RF frequency, and thereby the beam momentum, which in turn transforms into a transverse beam position modulation due to the dispersion of the G straight section where the target is located. Preliminary results with this scheme are encouraging. Under ideal conditions, we observe as little background as with the wiggling ribbon target, while the average luminosity and dead time look somewhat better due to the larger wiggling frequency possible in this case.

Finally, in a third mode of operation, we have scattered protons from a carbon micro-ribbon by slowly sweeping the beam across the ribbon. We found average luminosities about a factor of two lower than in the cases described above, nearly independent of the beam sweeping velocity which was varied between 0.12 and 0.41 mm/s. Furthermore, we observed considerably more background scattering in this mode (although spatially well separable from target scattering), indicating that beam cooling may not be as effective in this case.

In summary, we have established the feasibility of micro-ribbon internal targets for the Cooler. We are planning to study in more detail all three methods described above, and to determine their relative merits for various experiments.

B.2.3. Skimmer Targets

An important way to expose a target to a stored beam is to intercept the tail of the transverse distribution with a relatively thick target. The target (skimmer) in this case represents a constraint on the ring acceptance; it consequently reduces the lifetime of the beam and (if this process occurs over a time that is short compared to the beam lifetime without the skimmer) all stored beam is eventually lost due to its presence, i.e., all stored particles will have passed through the target. The event rate in a given experiment can be adjusted by controlling the distance of the beam from the edge of the target. The efficiency with which the stored beam is utilized is then the probability to obtain a trigger from a beam ion passing through the target. If it is acceptable (from the point of view of energy resolution) to choose a thick target, this efficiency can be made rather large. This method is equivalent to the slow extraction of the stored beam. It is important to realize that a heating-cooling equilibrium with the target is not established in this case. We have made use of skimmer targets to obtain background-free samples of events for detector testing, to investigate transverse beam distributions, and to measure the polarization of the stored beam.

A series of tests with various skimmer targets have yielded the following results. Protons that interact with the target can be distinguished from background events by localizing their origin (using the wire chambers for tracking) as well as by their substantial energy

loss in the skimmer. The contribution of background events is found to be at most 1 to 2%. The rate of protons scattered from the skimmer is expected to vary with the inverse square of the distance from the beam axis to the edge of the skimmer. This is a consequence of the shape of the transverse tail which is populated by Rutherford scattering from residual gas nuclei. This has been verified experimentally with 45 MeV cooled protons. The efficiency, i.e., the probability with which a beam ion is scattered into the detector, has been investigated with 120 MeV cooled protons. In this study the cylindrically symmetric CE01 detector accepted scattering angles from 4° to 17°. Graphite skimmers between 0.05 g/cm^2 and 1.63 g/cm^2 thickness were used and efficiencies between 10^{-4} and 10^{-3} were measured. For the thicker skimmers it was found that the yield critically depends on the angle between the beam and the edge surface. This is explained by the fact that only the first few 100 μm of the skimmer (measured from its edge) contribute to the luminosity. A computer simulation of the beam interaction with the skimmer, including multiple scattering in the target material, qualitatively reproduces the dependence of the efficiency on the skimmer angle.

Skimmers have become the target of choice for the routine operation of the CE01 detector as a polarimeter. In order to optimize data taking, the beam is moved locally towards the skimmer in such a way as to maintain as high a count rate as is compatible with limits on the data acquisition rate. A typical sequence of events through an experimental cycle is shown in Fig. B4. After completion of the stacking ("Stack"), the beam is captured into an RF bucket and cooled (increase in signal from the wall gap monitor). During this time ("Prep"), the wire chamber high voltage is increased to the operating level and data taking is enabled. By ramping down the trim coil current in the two dipoles adjacent to the G section, the beam is moved towards the skimmer edge and counting begins ("Count"). Eventually, the stored beam is used up, the initial parameters are restored and a new cycle starts ("Next").

B.2.4. Microparticle Targets

In addition to fiber and skimmer targets, microparticle beams are yet another way to provide solid targets of an appropriate thickness for Cooler experiments.

Difficulties with early efforts to accelerate charged microparticles by means of static electric fields were described in last year's annual report[1] where it was also reported that an alternate scheme that does not make use of electric fields had been shown to work in principle. In this new scheme the dust particles are mixed with a carrier gas at about atmospheric pressure. A stainless steel capillary tube of about 0.4 mm diameter connects the mixing cavity to vacuum. The gas flow through the tube accelerates the microparticles by Stoke's friction and focusses them by the Bernoulli force, caused by the approximately parabolic radial velocity profile of the flow in the capillary. At the exit of the tube the carrier gas expands suddenly while the particles continue unaffected because of their inertia, giving a well collimated beam.

We have continued to improve the performance of this system and to develop most of the necessary ingredients of a reliable working target[4]. In the near future we plan to test a target of this type in the Cooler ring.

The following aspects of the apparatus have received the most attention during the

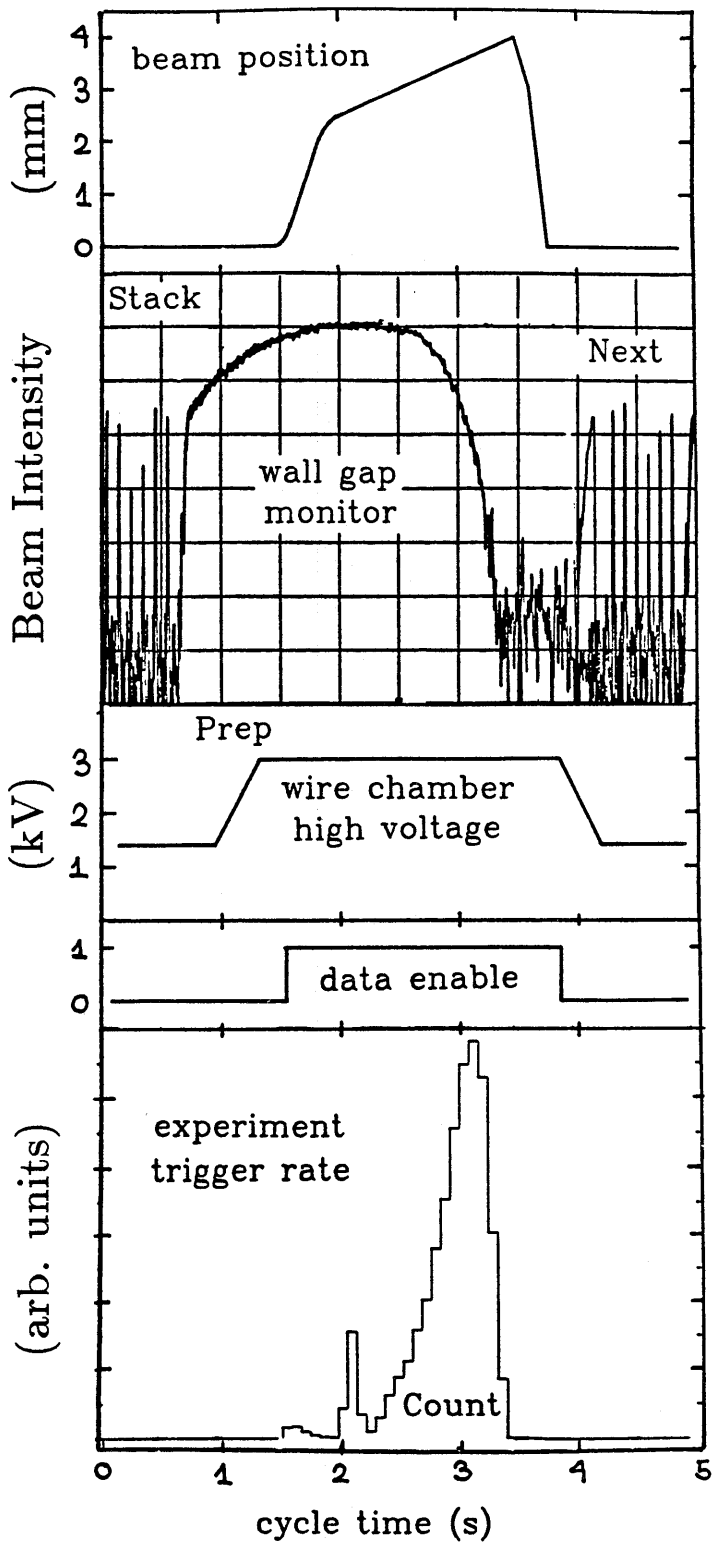

Figure B4. Time sequence within a beam cycle during a polarimeter run using a skimmer target. The details are described in the text.

past year.

- A homogeneous mixture of the micron-size particles with the carrier gas is crucial to ensure a stable, high-density dust beam. Good results were obtained when using a cylindrical mixing cavity made from lucite with a 0.013 mm Kapton-foil membrane at the bottom end. This membrane was exited by a resonant AC current through a coil attached to the membrane and centered around a permanent magnet (see Fig. B5).
- Clogging of the tube has to be prevented. Our attempts to avoid aggregations of dust particles from settling on the tube intake, either by shaking the tube or by protecting the intake by a mesh-grid, were not satisfying. This problem was solved as shown in Fig. B5. The capillary now is positioned in the center of a larger tube which also serves as the opening to supply the carrier gas. The oscillation of the membrane pushes the gas back and forth through this tube and thus produces an alternating flow parallel to the capillary, which prevents the settling of dust particles on the intake opening.
- Because of the stringent vacuum requirements in storage rings, a differential pumping system is necessary to separate the carrier gas from the particle beam. Such a system has been designed and tested.

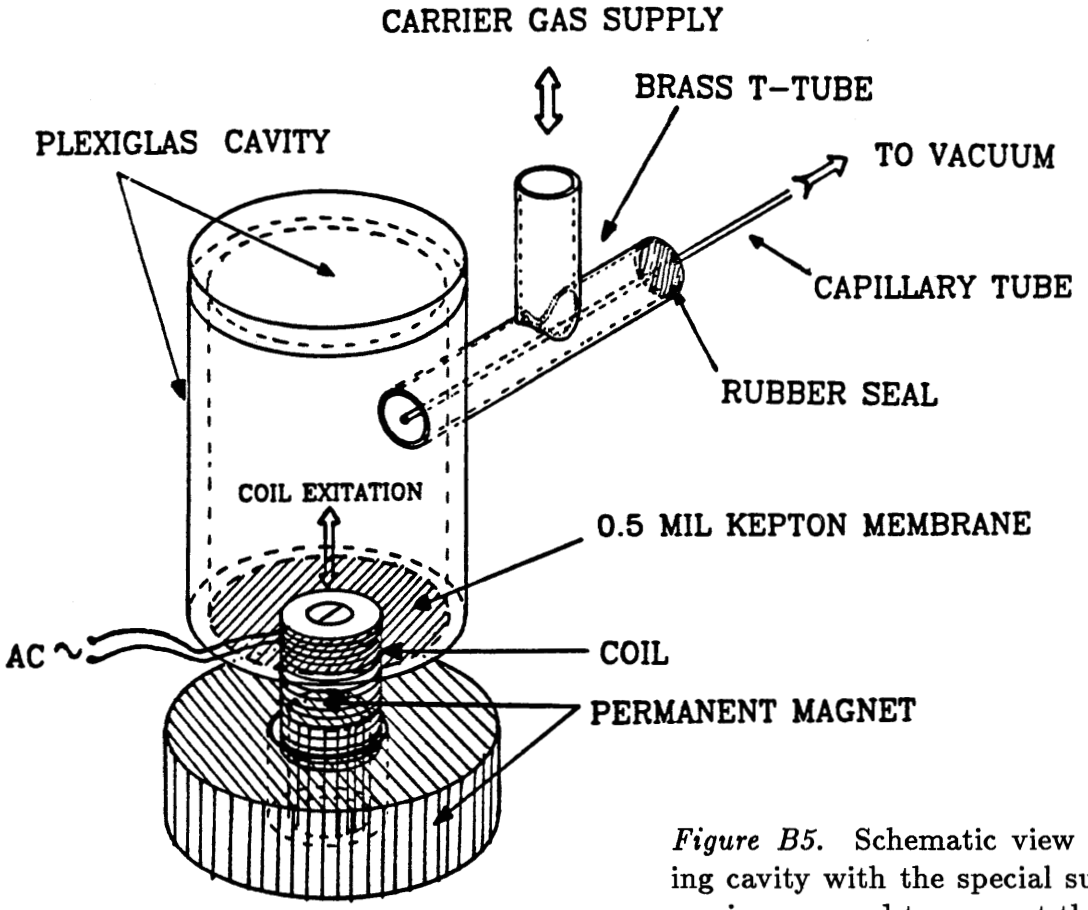

Figure B5. Schematic view of the mixing cavity with the special supply of the carrier gas used to prevent the settling of particle clusters on the intake of the capillary.

- Collecting the dust beam after its interception with the stored ion beam has to be very efficient since a relatively large amount of dust is needed and the pollution of the ring vacuum enclosure by microparticles has to be kept as low as possible.
- The behavior of the dust-gas system, i.e., its dependence on the particle material, choice of carrier gas, and tube parameters, needs to be understood quantitatively in order to allow an optimization of the performance of the target.

a) Dust Beam Diagnostics and Theoretical Work

To estimate the target thickness it is essential to know the velocity, v, of the particles and the width, Δx, of the dust beam, where it intercepts the ion beam. Assuming good collection efficiency, it is easy to measure the average mass flow J_m per unit time by weighing the amount of dust collected in a given time. Then, the geometrically averaged target thickness is

$$\rho = \left(\frac{J_m}{v \cdot \Delta x} \right). \tag{3}$$

The properties of the dust beam were investigated by Mie scattering of laser light. The test setup, as described earlier,[4,5] is shown in Fig. B6. The light from a 25 mW argon laser is focused onto the interaction region. The passing laser beam is then dumped while light scattered at forward angles from microparticles is focussed by two lenses onto the cathode of a photomultiplier. Pulses from individual particles are processed electronically.

To measure the profile of the dust beam, the laser beam can be moved up and down by means of an 'optical flat' (plane parallel glass plate of 14 mm thickness). The angle of the flat and thus the laser beam position are controlled by a stepping motor interfaced via a Keithley Digital I/O module (see Fig. B6). Typical scans of microparticle beam profiles

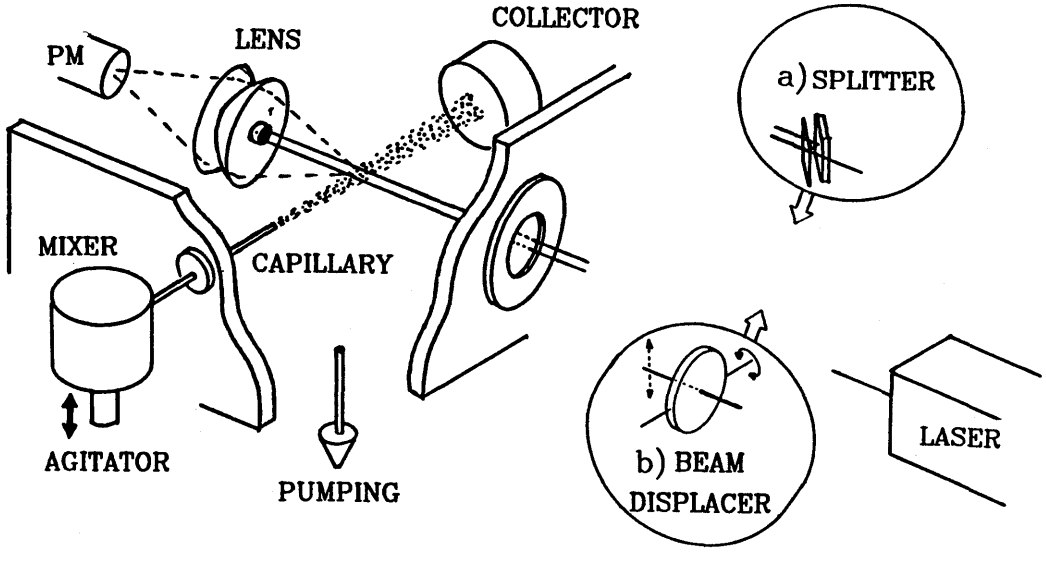

Figure B6. Dust target setup without the differential pumping system. Shown is the diagnostic laser beam with the options to a) measure the particle velocity and b) scan the beam profile.

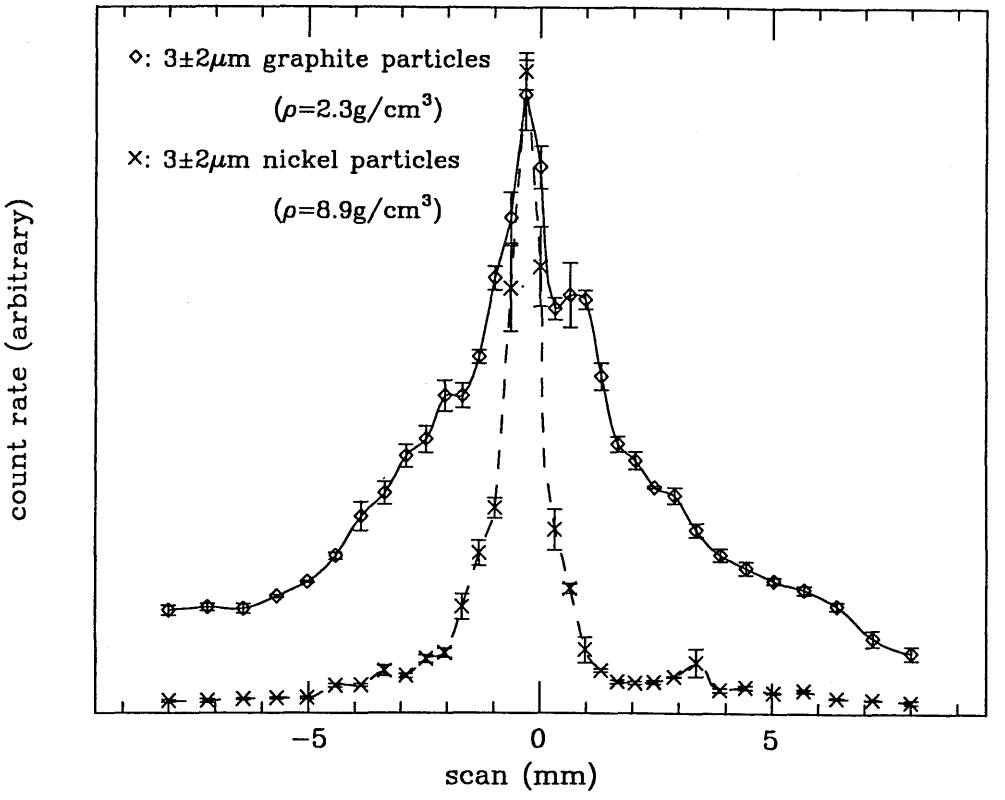

Figure B7. Microparticle beam profiles measured 63 mm downstream from the capillary exit. The carrier gas is nitrogen; the tube used is 61 cm long with an inner diameter of 508 μm.

obtained by this technique are shown in Fig. B7. The motion of the laser beam as well as data processing is controlled by an IBM personal computer. Software was developed in order to automate these measurements.

This setup also allows us to measure the velocity of individual microparticles by splitting the laser beam (see Fig. B6). The laser beam profile as well as the distance between the split beams was obtained from a scan with a P-N junction Silicon photocell mounted behind a 10 μm wide slit. The particle velocity is then deduced from the time of flight of the particles between the two beams. This has to be done at low particle flow rates to keep the average distance between two particles large compared to the beam separation.

Measurements[4] for different tubes, particle materials and carrier gases showed particle velocities in the range 100-300 m/s. The velocity distributions turned out to be rather broad and theoretical calculations (see below and Fig. B8) suggested that this is due to the particle size distribution of commercially available dust. To prove the dependence of the velocity on particle size, we measured the velocity distribution for 1 μm and 3 μm polystyrene spheres, advertised to have a size deviation of less than 1% (see Fig. B9).

For the theoretical modelling of the apparatus, we have assumed a one-dimensional, compressible, laminar, adiabatic gas flow. At our conditions the flow is choked, i.e., has

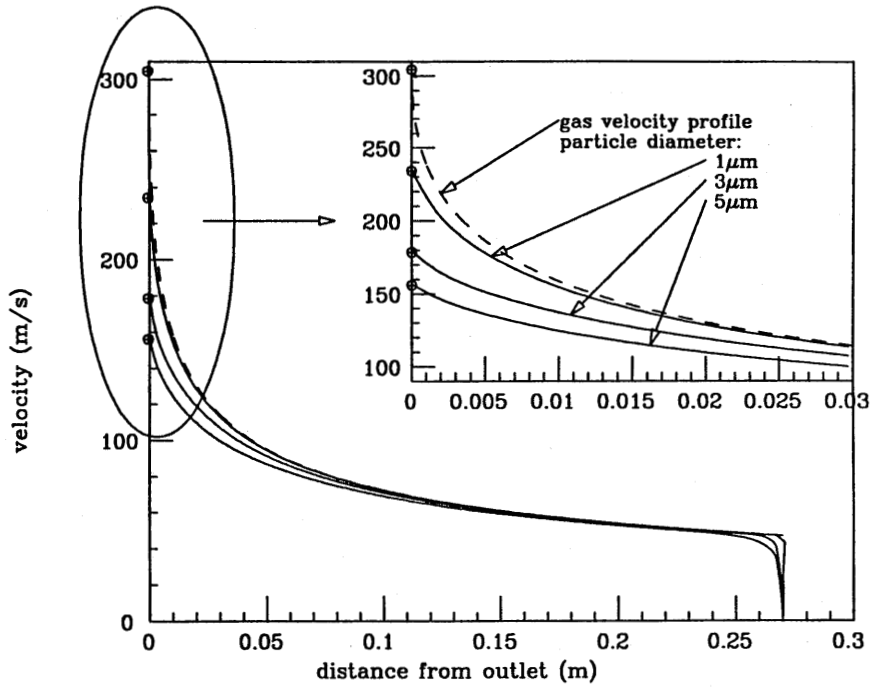

Figure B8. Calculated gas and particle velocity profiles for graphite particles in nitrogen for a 31 cm long tube with diameter 400 μm. The effect of the inertia can be seen, as the more massive particles cannot follow the quickly accelerating gas close to the tube exit.

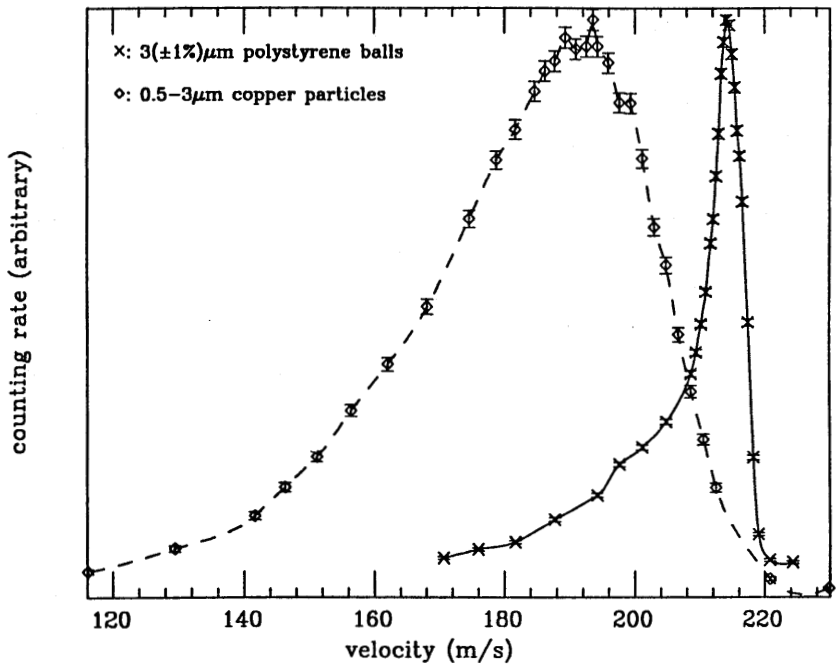

Figure B9. Velocity distributions measured with a 31 cm long tube with a diameter of 400 μm, using nitrogen as the carrier gas. The effect of the particle size can be seen clearly.

Mach 1 at the tube exit. This establishes the gas velocity and temperature everywhere along the capillary. The calculated total gas flow was found to be in agreement with measurements. Knowing the gas parameters and assuming a spherical shape for the particles, we calculate the viscous drag force and numerically integrate the equation of motion for the particles from the intake to the outlet. The calculations also account for changes of the viscosity with temperature and the adiabatic transition from an imaginary stagnation point inside the mixing cavity to the inlet of the capillary. The results were in reasonable agreement with the experimental data (Table I) and revealed some insight in the dependence of the particle velocity on the particle size and material, the gas and tube parameters. The strong dependence of the particle velocity on the gas reflects mainly the variation of the speed of sound for different gases, since, in this model, this is the velocity the gas reaches at the capillary exit. As shown in Fig. B8 the particles follow the gas until the steep rise of the gas velocity close to the exit, where they are, due to their inertia, separated from the gas. Thus, thinner tubes with steeper gas velocity gradients close to the exit lead to smaller particle exit velocities. The length of the tube is less important, but longer tubes give smaller particle velocities for the same reason (see Table I).

b) Differential Pumping System

Apart from the promising results of the bench tests, the one development needed before the installation of an operational dust target in the Cooler ring is the construction of a differential pumping system to remove the carrier gas. A test setup was built (see Fig. B10) to study our ability to operate a microparticle target within the vacuum requirements of the Cooler ring. The mixing cavity, as described earlier in this report, is mounted on a support rail inside a cylindrical vessel within which the pressure and gas composition can be regulated. The capillary tube ends within the first stage of the differential pumping arrangement. This first stage is pumped from the side by a Roots blower (M-D Pneumatics 5514-90L2) backed by another, smaller Roots blower (Leybold WS400) in series with a rotary vane pump (Leybold D60A). In order to protect the pumps from dust contamination, we constructed an S-shaped pumping line. As expected, the inertia of the particles prevents them from reaching the pump and a large amount of dust is trapped at the first bend. A skimmer opening separates the first from the second stage. The diameter of this skimmer as well as its distance from the capillary tube is chosen to optimize the ratio between microparticle and gas throughput. The second stage is pumped by a 500 l/s turbo pump (Balzers TPU510) from above a buffer chamber mounted on the side of the setup (not shown in Fig. B10). This chamber is used to protect the pump against dust contamination. The parameters of the second skimmer, separating the apparatus from the ring vacuum, can also be adjusted. Fig. B10 also shows a dust catcher inside a chamber, pumped by a 1500 l/s turbo pump (Balzers TPH1500). A Tee in front of this pump will not only provide an adequate protection against dust contamination, but will also provide enough space to mount the actual microparticle catcher. The present setup allows us to probe the microparticle beam with our diagnostic argon laser setup. The geometry of the flanges is such that the test setup easily transfers to the target chamber in the G-section of the Cooler, where it will be tested with stored protons in the near future. When used in the Cooler environment, the space beyond the second skimmer will become a third differential pumping stage with pumping apertures along the Cooler ion beam axis. The latter not

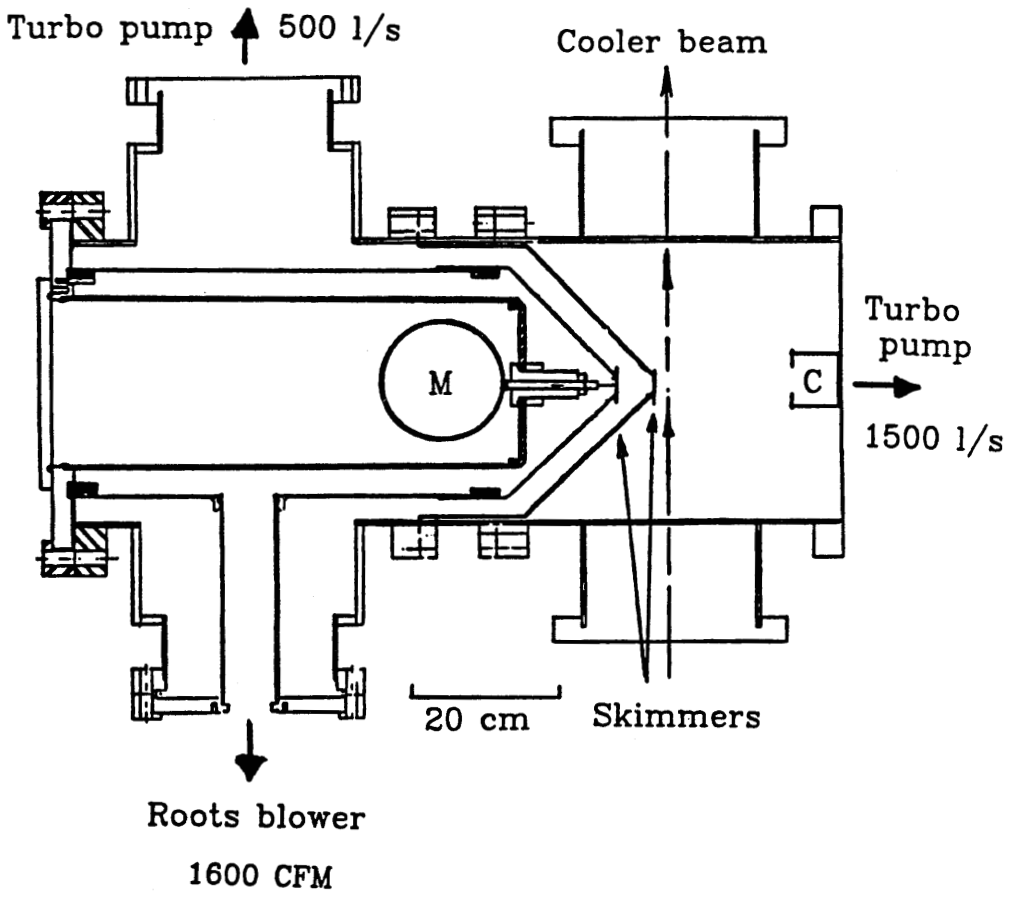

Figure B10. Setup used to study the differential pumping system. In the mixing cavity (M) the type of gas and the pressure can be varied. Different capillary tubes may be used interchangeably. The skimmers separate the stages of differential pumping needed to remove the carrier gas from the microparticle beam. The particles are collected in a catcher (C) whose shape has been optimized for maximum collection efficiency.

only separate the target region from the vacuum in the remainder of the machine but also serve as additional protection of the ring interior from any dust contamination.

c) Experimental studies of the gas-dust system

Since January we were able to use the test setup described in the previous section and shown in Fig. B10. Initially, only one pumping stage was implemented.

We investigated the dependence of the dust beam divergence, the pressure beyond the last pumping aperture, and the collection efficiency of the catcher on the tube design, the skimmer-tube configuration and the particle material. The collection efficiency is defined as the amount of dust caught with a 'standard catcher' divided by the total amount of dust exiting the tube. It was found that the pressure in the first pumping stage, typically in the 100 mTorr range, has no measurable effect on the beam width, suggesting that the divergence probably results from the drag from the quickly expanding gas at the tube

outlet. This is supported also by the fact that longer, thicker tubes in comparison to shorter, thinner tubes with the same gas flow give less divergent dust beams, since at the outlet the gas density and the drag force (which, close to the molecular flow regime, is expected to scale with the density) is smaller. In addition, denser particles give less divergent beams (see Fig. B7) which can be explained as an inertia effect, since the heavier nickel particles are less sensitive to a transverse impulse due to the expanding gas. The attractive magnetic interaction of the ferromagnetic Ni dust was ruled as the cause for the reduced beam width by reproducing the same effect with copper powder, which has almost the same density as nickel.

The pressure of the order 10^{-4} to 10^{-5} Torr in the laser beam region behind only one differential pumping stage is determined by the skimmer diameter and the gas flow through the capillary. In any case, the gas density there is so low, that it has no effect on the dust beam parameters.

Changing the skimmer diameter d_s between 1 and 3 mm and the distance L from the tube exit to the skimmer, but leaving the opening angle α (defined by $\tan\alpha = d_s/L$) constant, we found that the change in the collection efficiency reflects mainly the portion of the dust which gets scraped away by the skimmer. For large angles α, the collection efficiency is constant and determined by the catcher. It can be as high as 97% even with a relatively simple catcher design.

Currently we are trying to improve the catcher. Since the particles have to be slowed down by impact on the walls of the catcher, it is important to understand the process of reflection of microparticles from surfaces. To this end, we have measured scattering angle distributions for different surfaces, particle materials and angles α of incidence with the setup shown in Fig. B11. The scattered dust particles are 'detected' by simply covering the accessible solid angle with adhesive tape. Incident dust particles stick to the surface; their number can be determined by densitometry. For relatively soft graphite particles the scattering is highly inelastic, resulting in scattering at very shallow angles (small β) even for incident angles as large as 70°. Copper and nickel powders give a broad distribution, covering angles from 0° up to the impact angle α. When constructing an efficient catcher, the main objective is to prevent backscattering (back *out* of the catcher). Thus, we plan to use gently bent tubes leading into a reservoir, allowing many successive scattering events with shallow impact angle to gradually stop the particles.

We are now able to produce beams of graphite, nickel and copper particles which give target thicknesses of the desired order of 10^{15} atoms/cm^2. To be able to use the dust target in the Cooler ring, the catcher has to be improved so that it is able to collect of the order of grams of dust per hour with very high efficiency. Further improvements include a feeding mechanism to continually supply dust to the mixing cavity which is needed for long term operation of the target apparatus.

1. Indiana University Cyclotron Facility Scientific and Technical Report 1987, ed E.J. Stephenson, April 1988.
2. H.O. Meyer, Proc. Workshop on Nuclear Physics with Stored, Cooled Beams, 1984, AIP Proc. No. **128**, p. 76.
3. H.O. Meyer, Indiana Cooler User Guide, 2nd edition, March 1988.

4. A. Berdoz, A. Heinz, H.O. Meyer, P. Pancella, T. Rinckel, A. Ross, F. Sperisen, and D. Young, Proc. 10th Conf. on the Application of Accelerators in Research and Industry, Denton, TX, 1988, Nucl. Instr. Meth **B40/41** (1989) 455.
5. Indiana University Cyclotron Facility Scientific and Technical Report 1986, ed E.J. Stephenson, April 1987, p. 116.

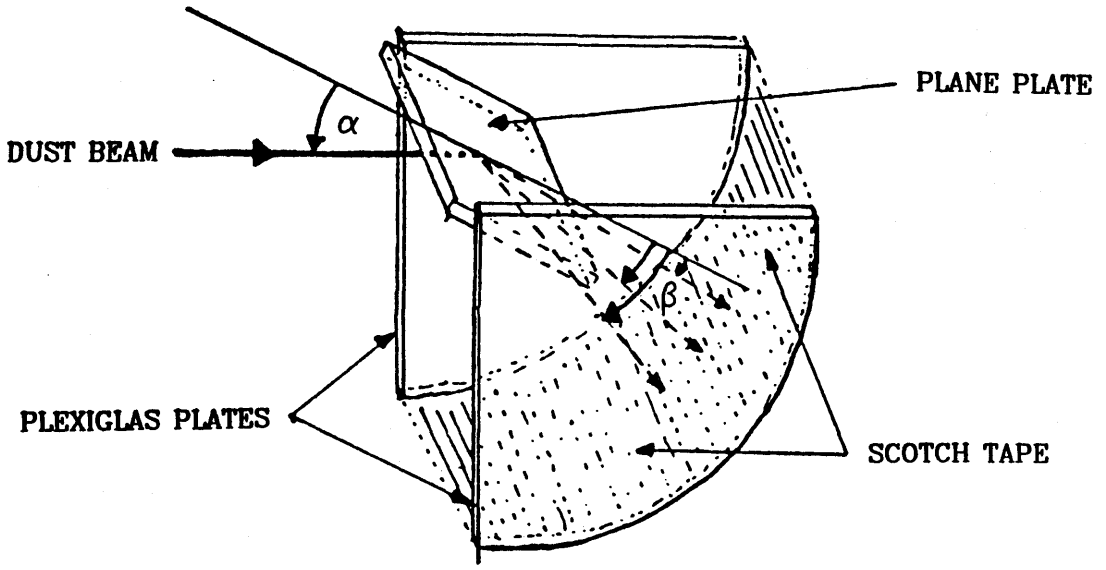

Figure B11. Device to study the angular distribution of scattering angles of dust particles reflecting from a planar surface with incident angle .

Table I. Comparison of theoretical predictions and measurements of the dust particle velocity. The measured velocity distributions are asymmetric and the sub- and superscript numbers give the half maximum half width in both directions. The overall uncertainty of the measurements is of the order of 10%.

PARTICLE PARAMETERS		TUBE PARAMETERS		GAS	VELOCITY DISTRIBUTION	
material	size (μm)	length (cm)	diameter (μm)		experimental (m/s)	theoretical (m/s)
C	3 ± 2	27	400	He	250^{+40}_{-50}	254
				N_2	180^{+20}_{-50}	179
				Ar	140^{+30}_{-40}	161
				SF_6	90^{+30}_{-40}	104
Cu	1	27	400	He	290^{+20}_{-80}	312
				N_2	210^{+10}_{-40}	200
		54	400	N_2	170^{+20}_{-30}	181
		54	200	He	130^{+10}_{-20}	125
				N_2	100^{+10}_{-10}	104

B.3. Progress with Experimental Equipment in the G Section

A. Berdoz, A. Eads, J.E. Goodwin, H.O. Meyer, M. Minty, P.V. Pancella, T. Rinckel, M.A. Ross, P. Schwandt, K. Solberg, F. Sperisen

B.3.1. Wire Chamber Efficiency and Plateau Data

Details of the construction and initial testing of the first wire chamber for CE01 were given in last year's annual report.[1] The design of the chamber is rather unusual, since it features a hole in the center that allows for the downstream beam pipe. A description of the design has been submitted for publication.[2] During the year 1988 a second, identical wire chamber was constructed and added to the CE01 setup. A third chamber that will serve as a backup is under construction.

Recently, part of one of the Cooler commissioning runs was devoted to a study of the efficiency and the plateau of the CE01 wire chambers. The detectors were arranged in the same order as shown in Fig. B1. The distance from the target to the first chamber (WC1) was 47.6 cm, to the second chamber (WC2) 94.5 cm, and to the E detector 108 cm. To investigate the dependence on beam energy, the study was done at 45 MeV as well as 104 MeV. A skimmer target was used because it produces background-free scattered protons. A 'good event' was defined by simultaneous scintillator pulses in exactly one element of each of the front and the E detector; a low cut was imposed on the energy deposited in the E detector. The condition for a valid wire chamber event was that, in any given plane, the wires that responded must be fewer than or equal to four and must be consecutive. The resulting efficiency measurements are shown in Figs. B12 and B13 for the individual chambers; the efficiency for getting a valid event in both chambers is also shown.

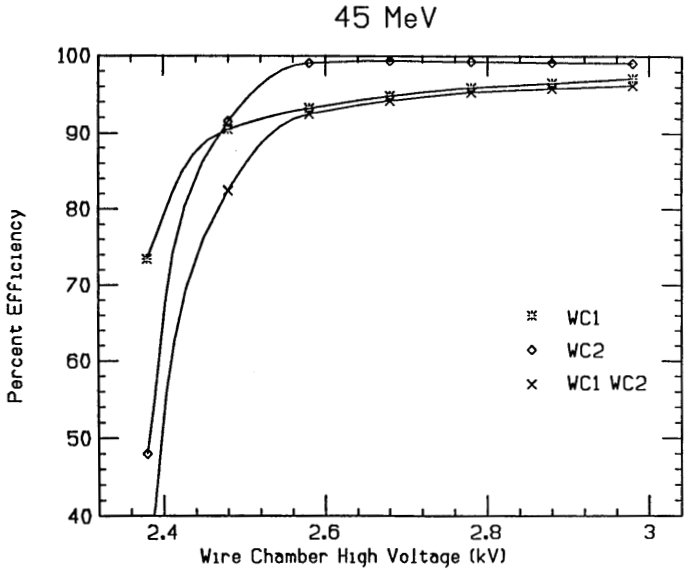

Figure B12. Wire chamber efficiency measured with 45 MeV protons as a function of the applied high voltage. Shown are the individual efficiencies for WC1 and WC2, as well as the logical AND between the two.

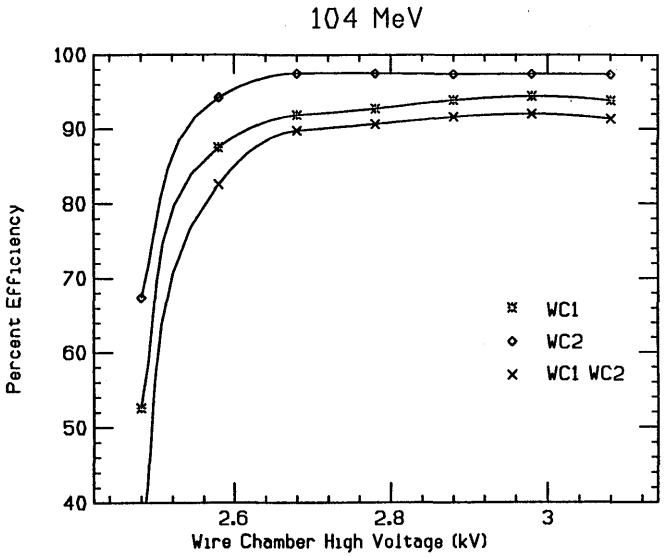

Figure B13. Same as Fig. B12 but measured with 104 MeV protons.

As can be seen from the figures, the measured efficiency is less than the expected 99%. For WC1 this is explained since there are particles that may well trigger the scintillators but that traverse through the hole in the center and thus miss the wire chamber. This geometrical explanation is supported by the fact that WC1 is less efficient at both energies.

From the measurements we also find that increasing the energy leads to a decrease of the efficiency. This is more clear for WC2 which is over 99% efficient at 45 MeV. It turns out that the events that do not contribute to the measured efficiency of WC2 at 104 MeV are not those that have no responding wires, but those that fire more than four wires. We have not been able to determine what mechanism is responsible for these multi-wire events; one possible explanation that reproduces the energy dependence involves delta rays produced by the proton that is being registered.

Until recently, the time-dependent chamber high voltage was supplied by a high voltage amplifier. This worked fine when ramping the voltage up and down as required by the Cooler running cycle. However, this supply did not protect the chamber from sparks or excessive current draw. In order to cure this problem, a Spellman high voltage supply with floating ground option was modified to provide the protection while ramping the high voltage. The circuit shown in Fig. B14 was attached to the high voltage output of the Spellman supply. The rise time of the pulse is given by R3 $\times$ C. The fall time is determined by the parallel combination of R1 and R2 in series with R3. We have chosen values that yield a rise time of 170 ms and a fall time of 340 ms. A trip circuit is attached to the current monitor on the Spellman supply. The trip point can be set between 4 and 20 μA. Since we started using this setup it has operated successfully; it has been verified that the protection actually causes the supply to trip off when left on during the filling cycle.

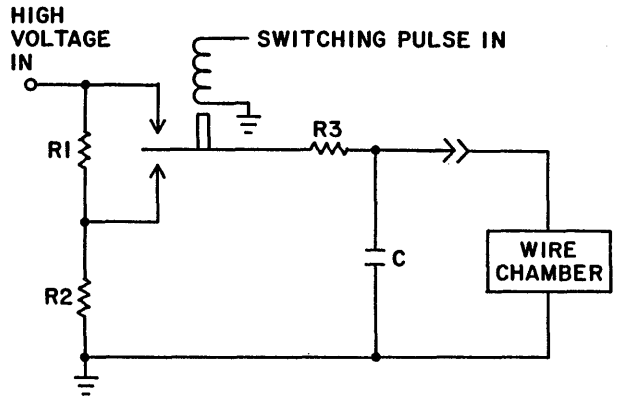

Figure B14. Schematic of the protective switching circuit for the wire chamber high voltage.

B.3.2. Particle Tracking

a) Introduction

The two multi-wire proportional chambers which have been built for CE01,[1,2] are identical in size and wire spacing, each consisting of two sense wire planes to measure orthogonal coordinates of position for a total of four planes. They were designed to be positioned back-to-back, both covering the same area transverse to the beam as the E-detector, both located relatively far from the target. The redundant information of the second unit, rotated 45° about the beam axis with respect to the other chamber, allows for ambiguities to be resolved in multi-prong events. This configuration provides the best possible scattering angle resolution if the origin of each scattering event is known, it is, however, not especially suited for particle tracking. If, for instance, the position of the scattering source is not precisely known, or the luminous volume is extended in space, then position information at two different distances from the target is required to track an event. For a given transverse resolution in each of the two planes, the tracking resolution (angle error) improves with increased separation between those planes. Therefore, one chamber should be much farther from the target than the other. Since we are dealing with a cone of acceptance with vertex at the target, it is obvious that the outer regions of the nearer detector will not be used if it is the same size as the detector farther from the target. The near chamber could be smaller, and the tracking precision would be improved if its wire spacing were correspondingly reduced. Even with these limitations, the tracking capability of the wire chambers has been extremely important in studying the CE01 detector performance and certain aspects of the Cooler beam.

Soon after the gas jet target was turned on[1] it was apparent that background events from sources other than the target gas were plentiful, and that some real geometric tracking would be essential in the development phase of the Cooler experimental program. We decided to use the existing wire chambers, but we mounted them on separate carriages so that they could be placed apart from each other. Aside from the primary goal of distinguishing background from real target events, good tracking data is also necessary for calibrating some aspects of the scintillation detector performance. For example, the light collection efficiency of the E-detector segments depends on position and angle of the track in the segment. The desired energy resolution is only possible with precise position

information at the E-detector. In addition, events close to the interface between the detector elements will have to receive special treatment.

b) Definitions

The necessary refinements in tracking became possible with the operation of solid targets in the Cooler (fibers and skimmers, see section B.2.) which provide clean, localized scattering sources. For the present purposes it is sufficient to note that with well-cooled beams, both types of solid targets can provide a scattering source that is virtually point-like, i.e., much smaller than the position resolution in all three space coordinates. There is also some control of the source location, both by moving the beam and moving the target. We are thus able to model the system and the various ways to analyze the data, predict what the resolution should be, what a point source should look like, and compare with real data.

Let us call the wire chamber which is closer to the target WC1, and the one farther away WC2. The two chambers are each adjustable in position along the downstream beam pipe anywhere between the F and E scintillators. The center of the ideal beam shall be the Z-axis, but for the purpose of tracking this axis is actually defined by the geometric centers of the two wire chambers, wherever they may be. We take the Y-axis to be vertical, increasing upward, and assume that the X sense wires in WC2 are parallel to this axis. The closest that WC1 can get is about 80 cm from the waist in the G section. WC2 is usually placed against the E-detector, whose active area determines the maximum accepted scattering angle (the latter may also be limited by the target position in relation to the thin exit window). The two chambers are typically separated by half a meter or more.

In all four coordinates, the wire spacing is 6.35 mm (1/4 inch). For events which fire multiple consecutive wires, the average transverse position resolution in each coordinate is actually better than plus or minus half of this wire spacing. There is a significant fraction of such events so that the average position resolution is close to ± 2 mm. Wire numbers from both chambers are recorded for every event which triggers the scintillators. The theoretical resolution transverse to the beam axis Z_0 from the waist is:

$$\pm s \times \frac{Z_1 + Z_2 - 2Z_0}{Z_2 - Z_1}$$

where the two wire planes are located Z_1 and Z_2 from the waist, and s is the transverse position resolution in each of the chambers. Using the observed fraction of 2-wire events, we predict that s should be 2.1 mm on average.

c) Position calibration

In order to achieve the best possible resolution it is crucial to precisely locate the position detectors with respect to a common reference frame. As far as possible, this should be done with scattered particles, although of course the detectors are initially surveyed in their positions rather carefully. Since both wire chambers have a central hole which admits the beam pipe with very little clearance, it is sufficient for our purposes to define the Z-axis as the line which joins the centers of the two detectors. Tests with beam on target for various chamber positions have shown that this axis passes within 0.5

mm of the ideal beam center horizontally near the waist of the G-section (with reference to the nearby beam position pickup PHG) and that when the detectors are moved they travel parallel to this axis within our ability to measure. Thus errors due to transverse displacements of the detector are negligible. The machine used to wind the sense wires is precise enough to allow us to assume the wire spacing is exactly 6.35 mm over the whole range of each coordinate. We assume the wires in each chamber are exactly perpendicular to each other. Small rotations about the X or Y axes have very little effect on position resolution. In the future such rotations will be kept small by measuring the Z-coordinate of each detector at three points allowing positioning of all planes perpendicular to the beam within about 0.1°. That leaves two degrees of freedom to be accounted for, position along the Z-axis, and relative rotation about that same axis.

Using a cooled 104 MeV proton beam sweeping into a carbon skimmer plate target, with the two chambers placed back to back, we were able to measure the angle of rotation between the wires of WC1 and those of WC2. The carriages are designed to fix this angle at 45°. The precise location of the target was determined from a run immediately prior, with the chambers separated (as described in the next section). Then, assuming that same target location, and an angle difference of 45°, the azimuthal angle ϕ of each track was calculated from each chamber, and the difference between the results from WC1 and WC2 was placed in a histogram. Fig. B15 shows that the distribution which resulted from over 16000 events was 1.7° wide but centered at −0.27°. This error has a small effect on position resolution (Fig. B16) and is easily corrected. It is also observed to persist in other runs, although this particular distribution is wider when the two chambers are separated in Z.

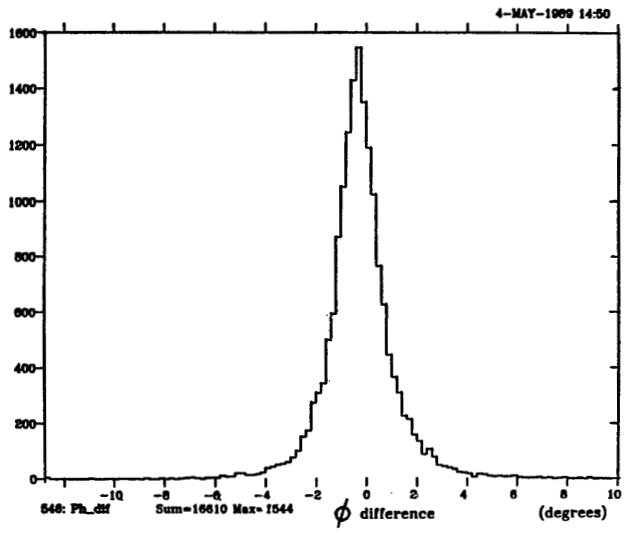

Figure B15 Difference in ϕ calculated from the two chambers back to back, assuming the relative rotation is exactly 45°. The centroid is −0.27° and the full width at half maximum is 1.7°.

The exact detector positions along the Z-axis affects resolution much more than other possible errors. It is, for instance, not sufficient to treat the two sense planes in a given detector which are separated by 22.23 mm (7/8 inch) as if they were located at the same Z-coordinate. A dramatic improvement in transverse tracking resolution is observed when this separation is taken into account (Fig. B17). Soon a positioning system will be installed to locate the chambers along the beam within about a millimeter.

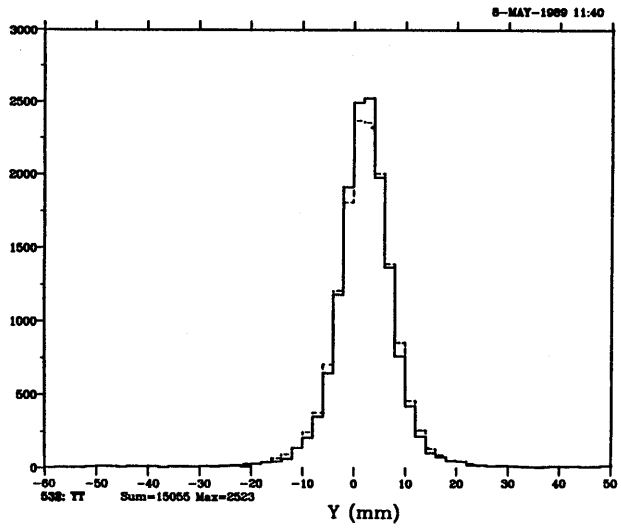

Figure B16. Comparison of transverse resolution at the target plane with and without the 0.27° correction in wire chamber rotation detected in Fig. B15. The Y-coordinate of points where the tracks intersect a plane transverse to the beam at the target is histogrammed for 15000 events. The solid histogram is calculated with the correction, the dashed histogram without. The dashed distribution is 5% wider than the solid.

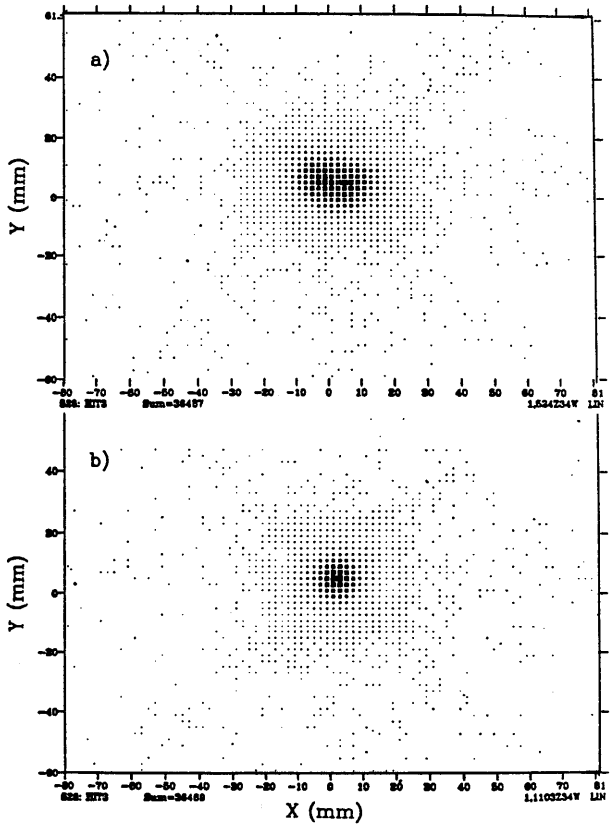

Figure B17. Comparison of transverse resolution at the target plane with and without the correction based on the sense wire plane separation in each chamber. For the same data, the intersection of every ray with a plane transverse to the beam at the target is plotted in two dimensions, larger squares correspond to more events on a linear scale a) assuming the same Z-coordinate for both transverse coordinates in a single chamber, and b) considering the 22.23 mm separation between sense wire planes.

d) Locating scattering sources

Thus far, we have studied elastic scattering which results in one detectable charged particle. With only one track per event, it is impossible to find the origin of the scattering without some assumptions. In all cases we have investigated, multiple scattering (e.g., in the 0.127 mm steel exit window) is small enough to be ignored; also, there are no significant magnetic fields along the particle trajectories. Thus, we may assume that the two points in space given by the wire chambers define a straight line which intersects the scattering source. We have used three different methods to deduce the location of the source in such circumstances.

The first method requires the fewest assumptions, but does require that a localized source exists from which we have recorded a large number of events widely distributed in scattering angle. We project the collected rays into a series of planes parallel to the detectors. As these planes get closer to the actual Z-coordinate of the source (target) the recorded events occupy a spot of decreasing size, centered at the XY coordinates of the source (Fig. B18). We fit the peak with a Gaussian in X and Y to quantify the width in order to find the Z location where the width is smallest (Fig. B19). Note, that the

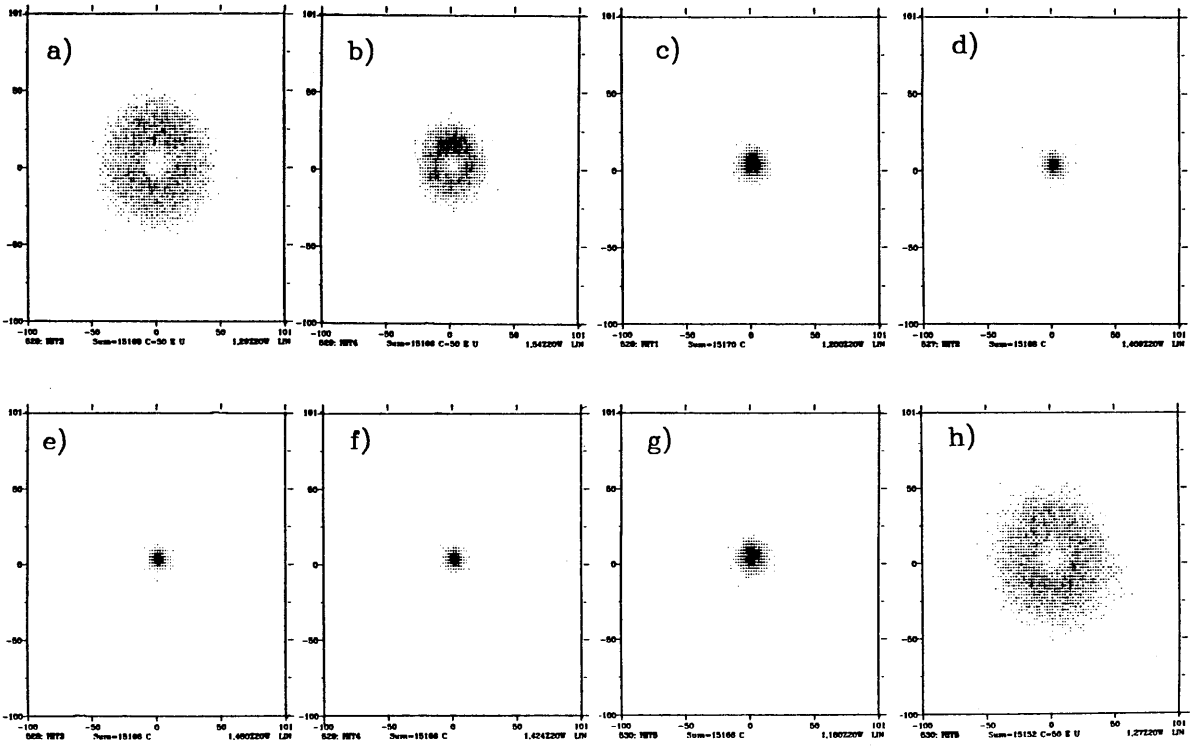

Figure B18. Illustration of the first method for locating a source. The intersections of all rays with planes located at various distances downstream of the waist in G are plotted, +Y is vertically upward and +X to the right as viewed by the beam, scales are in millimeters. The Z-coordinates of the planes are as follows: a) 50 cm, b) 45 cm, c) 40.5 cm, d) 39 cm, e) 37.7 cm, f) 37 cm, g) 35 cm, and h) 25 cm. Note that a) and h) are approximately the same distance from the target at 37.7 cm and show virtually the same pattern.

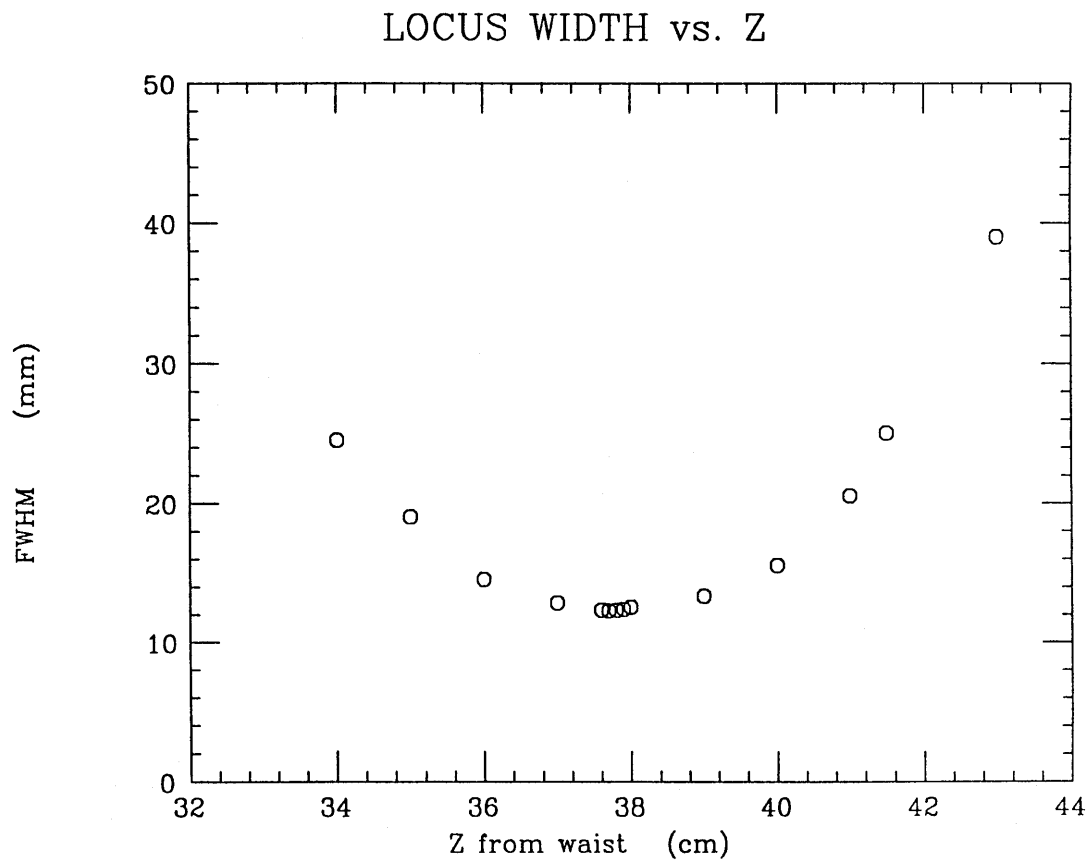

Figure B19. Widths of distributions (as in Figure 5) as a function of Z-coordinate. The minimum width is 12.5 mm and occurs at 37.7 cm downstream from the waist, which is within a few millimeters of the expected target location.

minimum width, about ±6 mm, is in good agreement with the resolution predicted above (Z_1 = 82.5 cm, Z_2 = 128.5 cm) which would be 6.2 mm in this case. A projection into the plane of the target is the best place to make a cut to separate real target events from background. While a circle of radius 7 mm in such a plane can contain almost 90% of the events from a point source target, any source separated by, say, 10 cm in Z from the plane of the target will spread its rays over a wide area in this plane. This method actually works for multiple sources too, if they are well separated in Z and close to the axis. This is because the central hole in the detector stack cuts out events with small scattering angles (assuming sources near the beam axis). This hole appears in the pattern of events from a single point source (Figs. B18 a, b, and h) in planes sufficiently far from that source; another source may become visible in that hole (Fig. B20).

A second method of locating a source is to calculate the scattering angle of each event in two different ways. Define the scattering angle relative to the Z-axis as determined by the detectors. We first calculate this scattering angle for a given ray, defined by the two points in the two detectors. For the same event we calculate that same angle, but

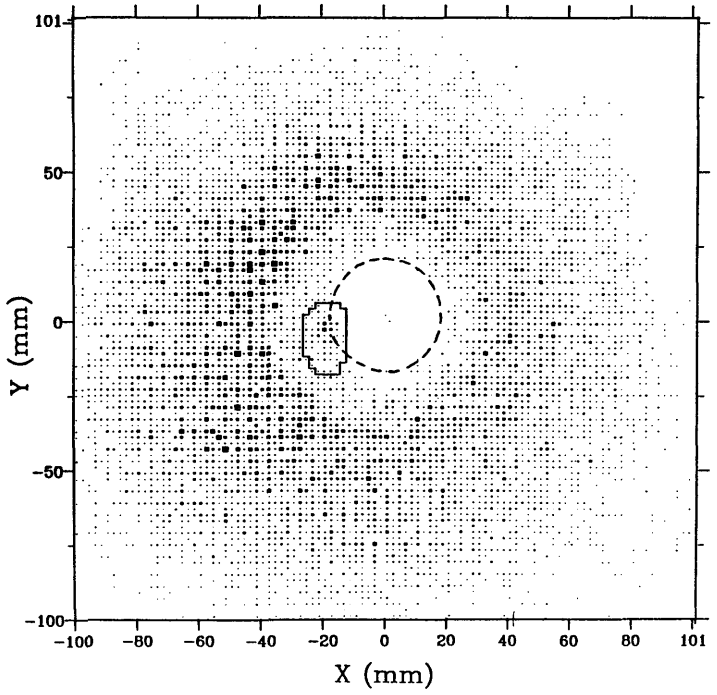

Figure B20. A secondary point source visible in a plane 29 cm downstream of the primary source (fiber target). The plane of this projection corresponds to the exit window on the chamber, which has a hole indicated by the circle where the beam pipe is attached. Events from the target appear outside a larger circle defined by the inner radius of the front scintillator which is nearby. Events inside the irregular box are apparently due to a low energy tail from the beam scattering from the edge of the hole in the target window.

this time defining the ray by the point in WC2 and an assumed target location. These two calculations should yield the same answer if the correct target position is assumed, so we histogram the difference for many events. Now the assumed target position can be adjusted until this difference is centered on zero. We generally use information from plane projections near the target (as above) to get the small displacements of the target in X and Y, and then find the Z of the target by this method (Fig. B21).

The third method is most useful for small data samples (even individual events) but requires the assumption that the only relevant sources come from a known beam location, and that the beam itself is parallel to the Z-axis defined by the detectors. For every line defined by the two detected points, we calculate the point where this line comes closest to the beam axis. This point is defined as the source, and we call the distance of closest approach d. If an interesting source is not on the assumed axis, the axis may be moved in parallel fashion to minimize d. This method is very useful for providing a quick distribution of sources in the Z-coordinate (Fig. B22) and events with large d are generally uninteresting background and may be safely cut by this method. The principal disadvantages are that off-axis sources give a distribution in Z which is biased by our limited angular acceptance,

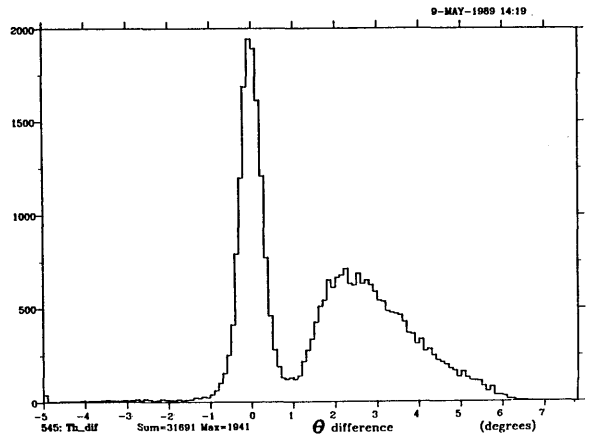

Figure B21. The θ difference method for locating a source, in a case of multiple sources. The narrow peak corresponds to events from the actual target whose location is input to the calculation. The difference displayed is scattering angle calculated from WC2 and the input target location, minus the angle calculated from both chambers. Therefore the broad peak to the right indicates another source upstream of the target, which is known to be the horizontal BPM at the upstream entrance to the target box, called PHG.

and the source deduced by this method for any non-zero d is not likely to be the true source.

A combination of these three methods may be used to locate scattering sources. The characteristic error in this system is a constant angle error, so the transverse resolution deteriorates with increasing distance from the detectors. The resolution for locating a source in Z by any of these methods deteriorates in the same way, but is also drastically affected by the accepted range of scattering angles. The larger the accepted scattering angle, the better any of these methods will work. Within the bounds of the target box

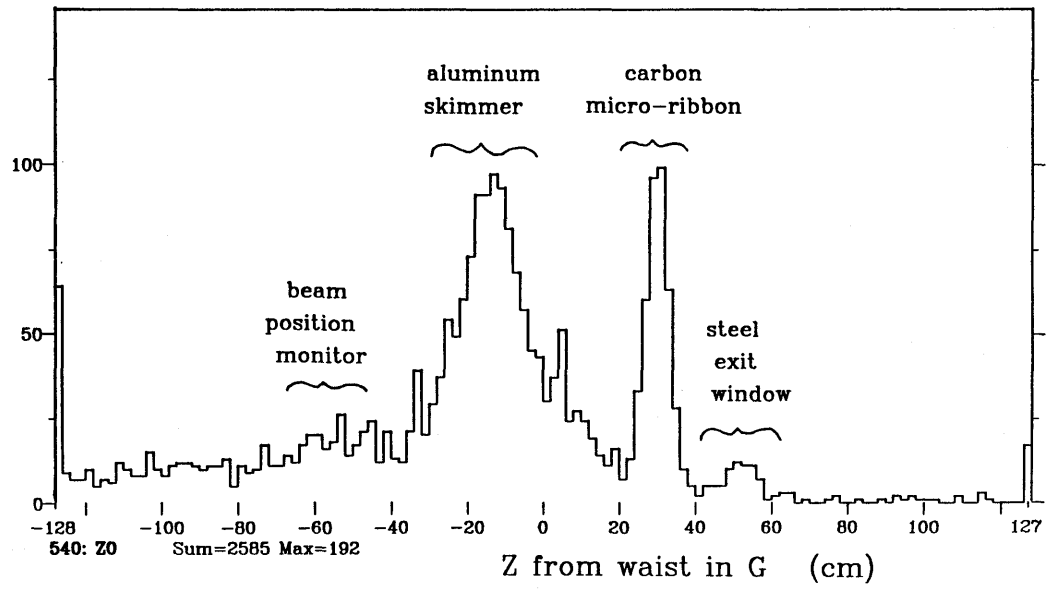

Figure B22. Histogram of Z-coordinate of closest approach to the beam axis. Four separate sources are actually visible here, from left to right: PHG at about −55 cm, an aluminum skimmer at −12 cm, the carbon fiber target at 30 cm, and the steel exit window at 55 cm.

in the G-section, and with optimum placement of the detectors, we are able to locate an isolated source within a centimeter or so along the beam, and better transverse to the beam. The condition for separating nearby sources is not that good, and at least 10 cm separation along the beam is required for resolving separate sources.

These methods in various combinations have given us powerful tools for locating background sources, isolating real target scattering, and comparing signal to background with various beams interacting with solid targets. When concerned about scattered particles from parts of the gas jet target, however, the resolution with the existing chambers is not sufficient to distinguish the nozzle of the gas jet target, which is nominally 6 mm from the beam, and we would have difficulty separating the closest pumping apertures, which were 7.5 cm from the target in the Z direction. When in the future multi-prong events will be available for analysis, the source position resolution will improve by roughly a factor of two, since we will be tracking the intersection of at least two measured rays.

B.3.3 Hardware and Data Acquisition Improvement

a) Electronics and acquisition software

The hardware of the CE01 detector system has changed little in the past year. A coincidence register was added to latch 'spin bits' at the beginning of each Cooler cycle. This is needed to indicate the status of the source when filling the ring with polarized beam. A scaler counting at 100 kHz, reset on each fiber crossing and read out on each event was added to time events relative to the motion of the fiber. A new beam current meter to be read by the experimental electronics was developed by the beam dynamics group and integrated into the acquisition system. A 'memory look up unit' which serves to select, in the trigger, desired patterns of the segments of the energy detector went through a final checkout. Recently, a persistent noise problem was traced to a coil of delay cable which was magnetically picking up noise from a fan motor. At this time the detector electronics is well understood and ready for use with experiments.

The software side of the CE01 detector has evolved considerably over the past year. With the corrected tracking of the wire chambers (see section B.3.2.), the E-detector gain correction (see below) and TOF correction (see below), the detector is becoming more and more useful as a tool for investigating many Cooler aspects.

The basic software system is comprised of a set of seven files used to set up XSYS (the standard IUCF data acquisition software). Three files are used to set up the programmable CAMAC modules, the detector high voltages and the Cooler cycle timing. Several files contain the parameters for offsets and gains; and a set of 'user- friendly' programs serves to manipulate CAMAC and XSYS. To maintain this growing group of files we have adopted a naming convention in which three letters designate the month and a single letter the version, i.e., MAYD.

The data acquisition path can be any of five different options, corresponding to individual event streams. Event-9 is a 'Begin' event which forces data acquisition to a proper start at the beginning of a Cooler cycle. This insures that the cycle clock, a scaler counting at 100 Hz and reset at the beginning of each cycle, is always correct. Event-8 is a scaler 'Read' which occurs at the beginning of every cycle, reading and clearing the scalers values

left from the previous cycle. Event-4, the 'Rate' event, occurs every 80 milliseconds and reads out selected scalers and sampling ADC's. This allows a deadtime free measurement of detector rates, beam current and other cycle-dependent parameters.

Event-5 and event-6 are the main data events for the CE01 detector. Their respective trigger conditions are defined within CAMAC programmable ECL logic modules. The event condition contains a combination of the discriminator outputs of the energy (E), front (F) and veto (V) detectors and a 'Fast Clear' depending on the status of a memory look up unit which reads the E detector segment pattern. Currently, event-5 is defined to be a double coincidence E·F, vetoed by V, and event-6 is defined as the triple coincidence E·F·V. These data events are about 50 words in length: 32 words are from the wire chamber coincidence registers, 6 are miscellaneous parameters (e.g., clocks) and the rest are FERA ADC's and FERA ADC's in conjunction with TFC's (for time of flight) which are readout in compressed block mode, suppressing the transfer of channels that contain a zero.

The analysis (EVAL) code in XSYS then sorts the event information into spectra. The event-4's are sorted such that spectra are incremented at the channel corresponding to the current cycle time by an amount equal to the difference in subsequent scaler readings. Thus, 'rate spectra' are generated that allow recording rates as a function of time after the start of a cycle.

Event-5 and event-6 are currently still sorted together (this will change for data acquisition in CE01). The EVAL code first decodes the FERA ADC's (and TOF's) block readout and the wire chamber bit pattern. Then a user accessible FORTRAN subroutine is called. This subroutine takes the raw data and calculates the parameters of interest for display. These parameters include the sum of the two phototube signals for each energy detector segment, the time of flight from different front and energy detectors, various corrections of the wire chamber outputs for actual wire plane positions, the calculation of virtual wire chamber positions (e.g., projecting rays back to the target plane), and the determination of the angle of the track. Corrections of energies and times of flight which depend on the position of the track are also carried out here. This subroutine will eventually handle two-prong events as will be detected in CE01. The subroutine also sets flags signifying validity of events. These flags are then evaluated with the condition table feature of XSYS. This makes it possible to sort only those events that pass the specific conditions listed in the condition table.

During actual data taking, event-5 and event-6 are 'sampled', i.e., only one in five events (for instance) is actually sorted into spectra. This limits the VAX CPU time to a reasonable value (around 10%) which is necessary to keep the dead time low enough so the rate events are always serviced. With sample sorting and writing to tape, a data rate of 200 Hz can be maintained with a live time of about 75%. During replay (no sample sorting), the MicroVAX can sort about 200 events per second.

b) Time of flight measurements

Because of the four-fold segmentation of the front detector and the eight-fold segmentation of the energy detector (with 2 tubes on each segment), there are 4 possible time-of-flight starts and 16 possible stops (not to mention 8 more veto detectors). This complexity is handled with a TDC on each detector (time to FERA converters (TFC's) connected to FERA ADC's). The start for all these TDC's is the AND of the OR of all

front segments with the OR of all energy detector segments. Adjustment of the coincidence overlap time can be made remotely through CAMAC.

For single-prong events, the software calculates the difference in time between the front detector that fired and the energy segment that fired (time average of both tubes on this element). Thus, a true time of flight is calculated. The problem is that each TFC-FERA channel can have a different offset, complicated by the fact that an energy segment overlaps several front segments. Thus, to align the various combinations, 12 adjustable time offsets (4 for the front segments and 8 for the energy segments) have been provided. After this offset correction, with the times of flight from all eight E elements in one spectrum, a time resolution of 0.8 ns has been seen. When accumulating TOF spectra for only those events that fall within an individual E gain correction bin (well localized within a given element) a time resolution of about 0.4 ns is obtained. Time of flight corrections that depend on position will be available in the future.

c) Cooler cycle timing

Because of the cyclic nature of Cooler experiments (repetitive filling, beam preparation data taking, etc.), new problems arise in the data acquisition process. The high radiation level that accompanies the beam spill during injection requires that the wire chambers be temporarily deactivated in order to increase their lifetime. The experimental conditions are changing throughout the cycle: cooling and acceleration take time at the beginning of the cycle and the beam current decreases exponentially due to beam losses.

A typical Cooler cycle for a non-accelerated beam starts with injection which can take from 0.1 seconds to 5.0 seconds depending on the type of stacking ('RF' or 'cooled') used. This is followed by about 1.0 second cooling time. Subsequently, the wire chambers and the target are activated and any beam manipulation needed for the target (i.e., a sideways motion into the skimmer target) is initialized. Then data acquisition is started. The cycle ends with data acquisition stopped, wire chamber high voltage off and target out in order to prepare for the next refill.

When accelerating, the cycle is extended between injection and cooling by the ramping of the beam energy which typically lasts a few seconds. Also, the cycle ends with the cycling of the magnets which is needed due to their hysteresis. This typically doubles the total cycle time.

d) Energy measurements with the E detector

The 10.2 cm thick scintillator of the E detector is designed to stop outgoing protons from the reaction $p+p \rightarrow p+p+\pi^\circ$ which is to be studied by the experiment CE01. In order to reconstruct the kinematics of the events an overall energy resolution of about 3% is required. Preliminary tests showed that two 12.7 cm diameter phototubes are needed with each of the eight sectors that make up the detector. These tests also showed that the desired energy resolution can be achieved if the variation of the light collection efficiency with the position of the incident ray is taken into account.

The use of skimmer targets (see section B.2.3.) made it possible for the first time to irradiate the detector with elastically scattered protons of well defined energy. Thus, data necessary to investigate the performance of the E detector became available and could be

used to carry out a position-dependent gain correction of the pulse heights measured.

The first step is to define a lattice, dividing the face of the detector into bins whose size is consistent with the variation of the light collection efficiency but still large enough for reasonable statistics. This is currently done by just using the wire numbers of the wire chamber, WC2, immediately preceding the E detector. Using the mono-energetic sample of protons, an energy spectrum is then constructed for each of the about 500 bins. The location of the peak in these spectra is taken as a measure of the collection efficiency from individual bins and a correction factor for each bin is deduced. The whole process is automatic and takes a few minutes. The resulting array of gain corrections is made accessible to the analysis program XSYS. On-line correction of the pulses from the E detector, based on the associated wire chamber information, is carried out in the XSYS user subroutine during acquisition or replay. A substantial improvement of the overall energy resolution of the detector (now 5.2%) was the result of this procedure (see Fig. B23).

In the future, the correction procedure will be improved by optimizing the binning pattern and by basing it on the track location projected into the E detector plane. A persistent noise problem was recently traced to pickup on delay cables for the analog pulses. Its elimination will further improve the energy resolution of the detector.

B.3.4. Recoil Detector for CE02

A large area parallel plate avalanche counter (PPAC) is being developed for use in CE02 (Pionic Atoms as Compound States in Nucleon-Nucleus Collisions). The PPAC will possess 2π azimuthal symmetry and is designed to detect recoiling ^{13}C nuclei of about 30 MeV. The PPAC signals will be used in coincidence with backwards scattered protons in order to be able to measure a small scattering cross section in the presence of a large background. Because the detector will be positioned downstream of the target, where the elastically scattered proton cross section is large, it must be capable of dealing with high count rates.

A prototype detector having an active area of 225 cm^2 has been constructed. Detector testing proceeded using isobutane gas and a ^{252}Cf source, which emits alpha particles and fission fragments. A careful study has been carried out of the detector response as a function of the electrode spacing d, the operating pressure p, and the applied electric field E. As an example of a typical measurement, we show in Fig. B24 the logarithm of the output pulse height as a function of the reduced electric field strength, E/p, for an electrode spacing of 3.6 mm. The pulse height, A, corresponds to the centroid of the alpha or fission fragment peaks in a pulse height spectrum. For reduced field strengths below 200 mV/cm/Torr the detector operates in the ionization region. The near-constant fission fragment output signal amplitude indicates that only primary ionizations in the gas occur. This plateau was not observed in the alpha particle curve because of longer radiation lengths associated with lighter particles. As the applied voltage is increased, the output signal amplitudes grow accordingly due to the formation of secondary ionizations.

Based on these offline tests, we established the following bounds on the operating conditions: the electrode spacing must be between the value at which surface effects lead to premature sparking and the value at which field inhomogenieties lead to position-dependent output amplitudes. The lower limit on the gas pressure is determined by the mean free

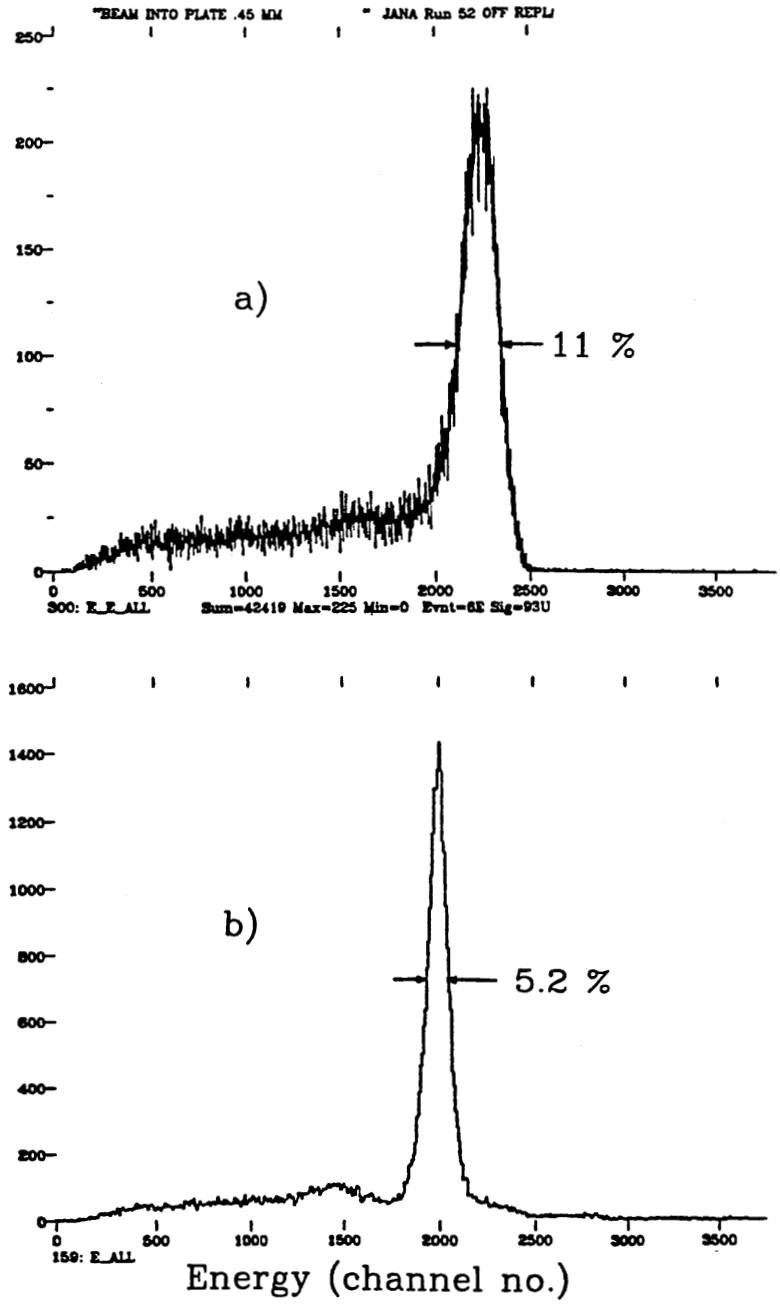

Figure B23. Overall energy spectrum obtained with the E detector with 108 MeV protons and a carbon skimmer target. Events from all eight segments are superimposed. The lower spectrum is obtained after position-dependent gain corrections have been applied.

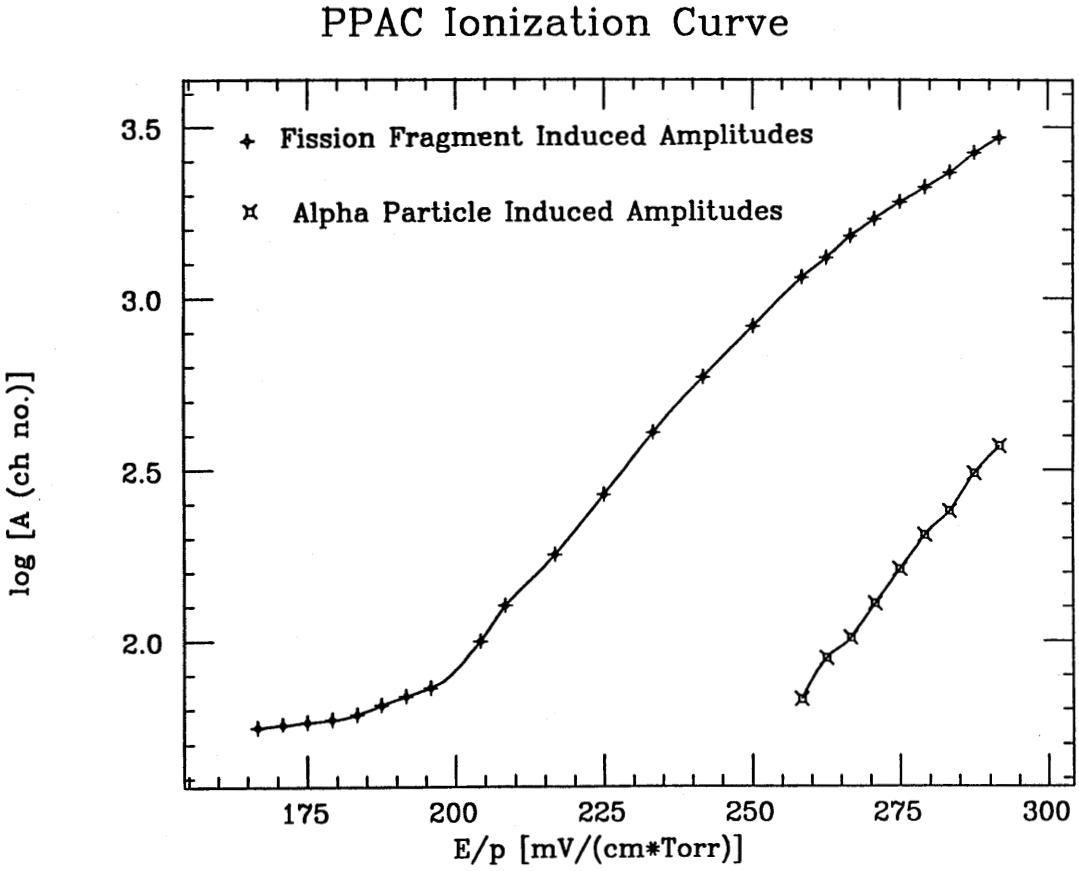

Figure B24. Ionization curve obtained with a prototype parallel plate avalanche counter. The electrode spacing was 3.6 mm and the counter gas was isobutane at 8 Torr pressure.

path between ionizations and the upper limit, for a given detector area, by the thickness of the foils on the detector housing. The applied field must be selected so that avalanches take place in the absence of electric breakdown of the gas. Analysis of the data dictates that the alpha particle induced signals are best resolved from those arising from the fission fragments at moderate electrode spacing (150 mil), high pressure (8 Torr, using 150 mg/cm mylar foils), and at high applied potential (850 V), just below the sparking threshold.

In preparation for online testing of the PPAC, it became evident that the high-frequency, small-amplitude Fourier components in the tail of the output signal had to be minimized, because timing jitter in the charge integrating ADC gate should not determine the PPAC energy. Signals resulting from improper grounding techniques were eliminated by a series of hardware improvements. A refinement of the gas flow control led to an increase of the sparking threshold and hence to an increase in the amplitude of the output pulse. Finally, coplanar PPAC coupling and mismatched impedances were accounted for by a more suitable choice of coupling capacitors and by proper termination of the signals, now taken from both planes. Following these modifications, the integrated charge was found to be independent of the inherent fluctuations in the timing gate.

1. Indiana University Cyclotron Facility, Scientific and Technical Report 1987, ed. E.J. Stephenson, April 1988.
2. Multiwire Proportional Chamber for the IUCF Cooler Ring, K. Solberg, A. Eads, J. Goodwin, P. Pancella, H.O. Meyer, T. Rinckel, and A. Ross, submitted to Nucl. Instr. Meth.

B.4. Progress Report on T-Site Construction for Experiment CE03

W.W. Daehnick, S.A. Dytman, P.C. Li, S. Saha, J.G. Hardie, M. Yamazaki, L. Bland, W.W. Jacobs, and R. Oram.

B.4.1. Introduction

The T-site is located at the 6° bend of the Cooler ring. Seen from the target location, the beam aims at the 0° neutron exit hole in the north outside wall of the Cooler building. To the left and the right of the beam pipe there is a modest, but useful, amount of space to mount experimental apparatus. Proposal CE03, approved to study the reaction $p+p \rightarrow p+n+\pi^+$, aims at taking advantage of the 6° bend in the middle of the T region to separate charged particles of low magnetic rigidity and neutral particles from the circulating beam. The same position in the ring can also be used to separate particles of high magnetic rigidity from the circulating beam. They would leave the magnet vacuum chamber towards the right of the beam, as do small-angle neutrons. Following the CE03 proposal, four additional proposals have been approved that wish to take advantage of the T-site.

The experiment which prompted the largest modification of the initially proposed bending magnet aims at the detection of recoils from the (p,γ) reaction. This experiment plans to use the bending magnet as a spectrometer to detect the recoiling residual nuclei with high accuracy. These recoils will be deflected to angles as large as 54°, compared to the proton deflection angles of 20° or less anticipated for the $p+p \rightarrow p+n+\pi^+$ experiment. New pole faces were laid out similar to a typical spectrograph, in order to achieve good momentum resolution for the large angle recoils.

The magnetic field was calculated using the 3D code Tosca. The goal of the now-completed design was to permit good momentum resolution while maintaining a large acceptance angle. The proposed T-Site magnet has a vertical acceptance angle of 6.5° and a horizontal acceptance of 20°.

Another planned experiment, (the detection of a (p,Δ^{++}) reaction) requires detection of outgoing particles that exit the magnet to the right as well as to the left of the circulating beam. Hence, the pole face edges to the right of the circulating beam also have to produce carefully shaped fields. As a consequence of these considerations, the current design has magnetic pole faces of a greater horizontal width, and a more complicated shape than previously.

The 3D calculations had shown that, with the larger (12.7 cm) gap, a more massive return yoke was needed than initially proposed. The current construction uses a yoke cross section 35.6 cm deep and 45.7 cm wide. The curvature of the pole faces and the tapering of the yoke add considerably to the construction costs. The magnet, as now ordered, will

become a permanent part of the Cooler ring and will permit a wider range of experiments while still providing the very large solid angle initially proposed (see Fig. B25).

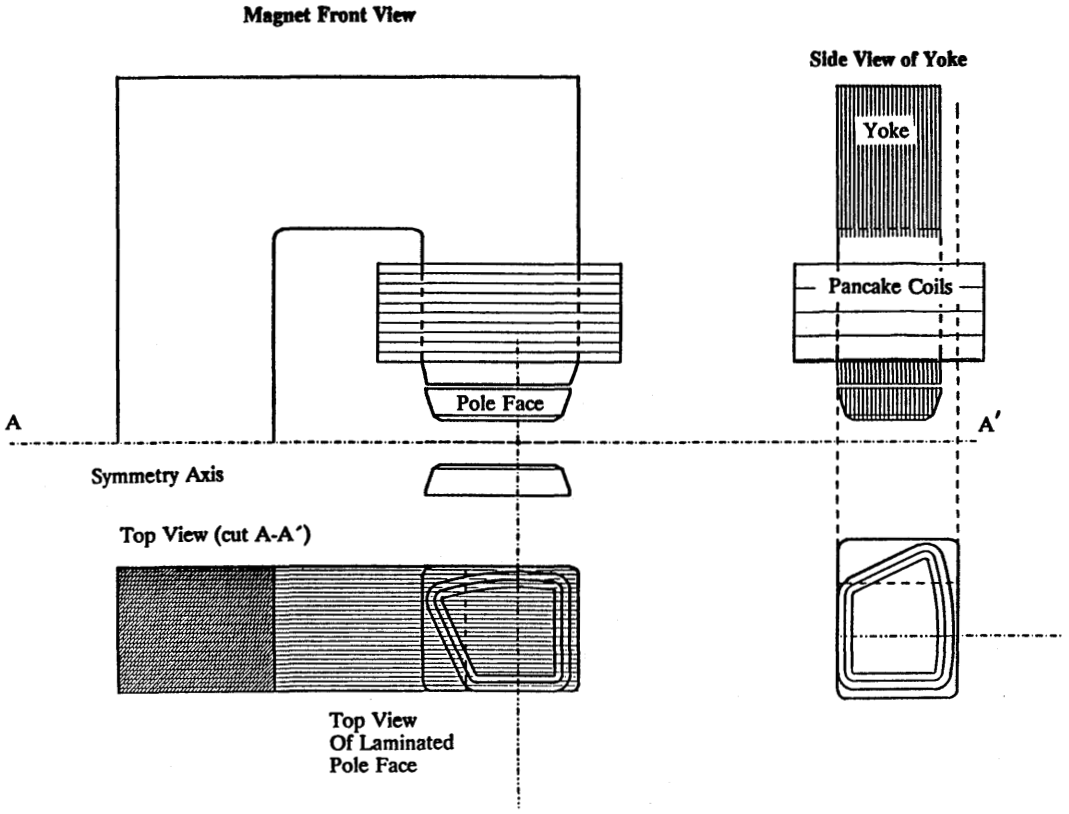

Figure B25. Front and side views of the new 6° magnet for the T section of the Cooler.

B.4.2. The Target

The target to be used for T-site experiments is the standard IUCF gas jet target to be run, initially, with hydrogen and deuterium. It will be located very close to the 6° magnet in order to permit the large acceptance angle desired. For CE03, the target center is located only 27.1 cm in front of the magnetic pole faces. This location of the jet has been frozen for design purposes; it can be accommodated by using a target chamber of the same dimensions as the one that is currently mounted in the A region of the Cooler. It is anticipated that this target chamber, together with pumps and other peripherals will be transferred to the T region.

B.4.3. Six-degree Magnet: Details

The new magnet is essentially a small-angle spectrograph which permits ejectile exit angles of up to 54° towards the inside of the ring and up to 30° towards the outside for positive particles of high rigidity, or for negative ejectiles. Figs. B26 and B27 show the top

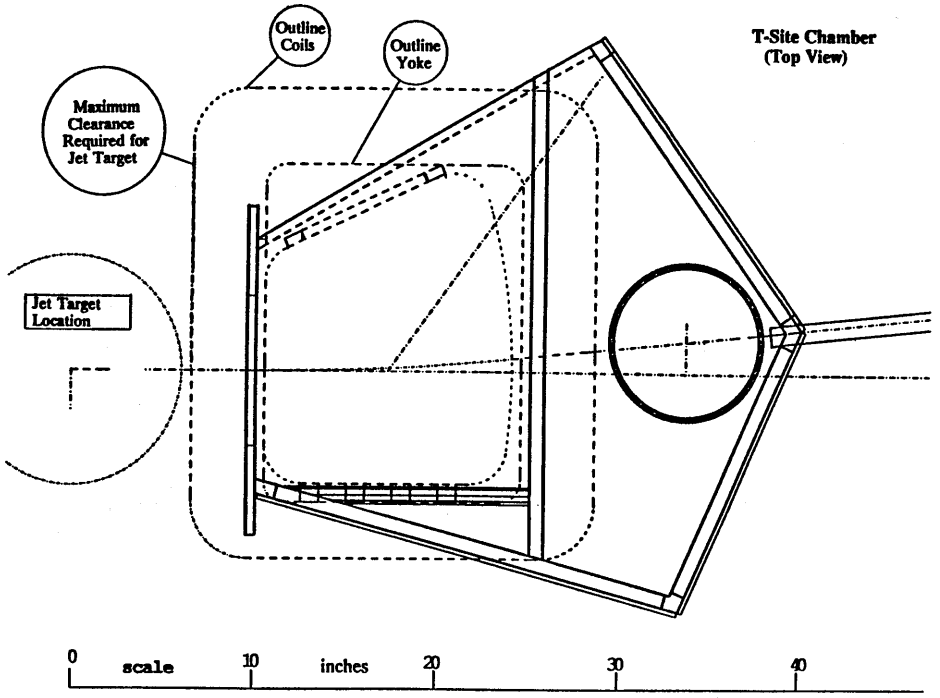

Figure B26. Top view of the new T section magnet. The outline of the yoke, coils, and pole tips are shown together with vacuum chamber assembly.

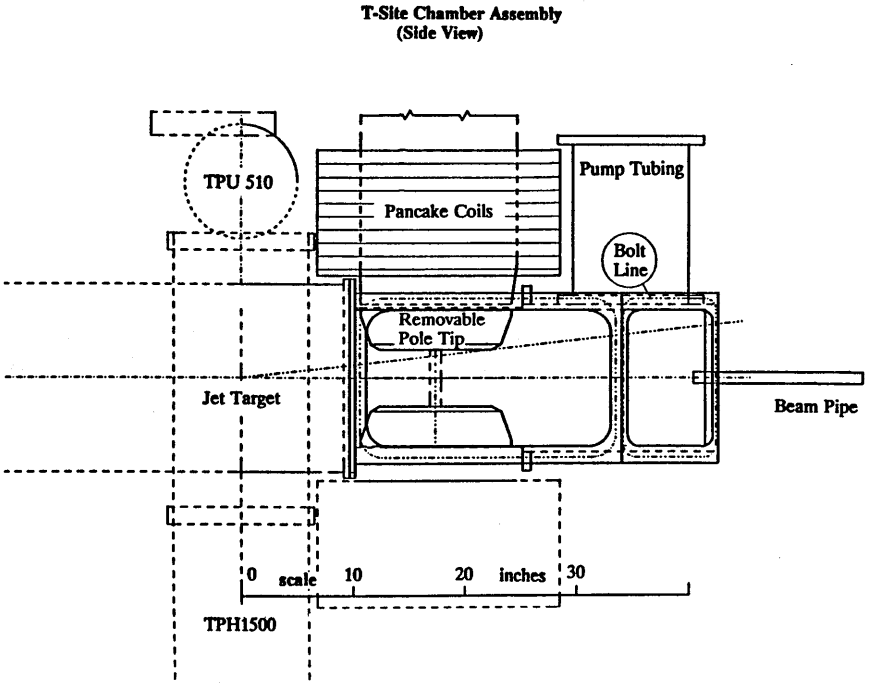

Figure B27. Same as Fig. B26, but side view (including pumping stations).

and the side view, respectively, of the magnet and magnet chamber as currently specified. The fully usable area of the gap is 33 cm wide by 12.7 cm high, over the entire length of 34.3 cm. A sketch of the magnetic field along the beam direction, as calculated by code Tosca, is shown in Fig. B28.

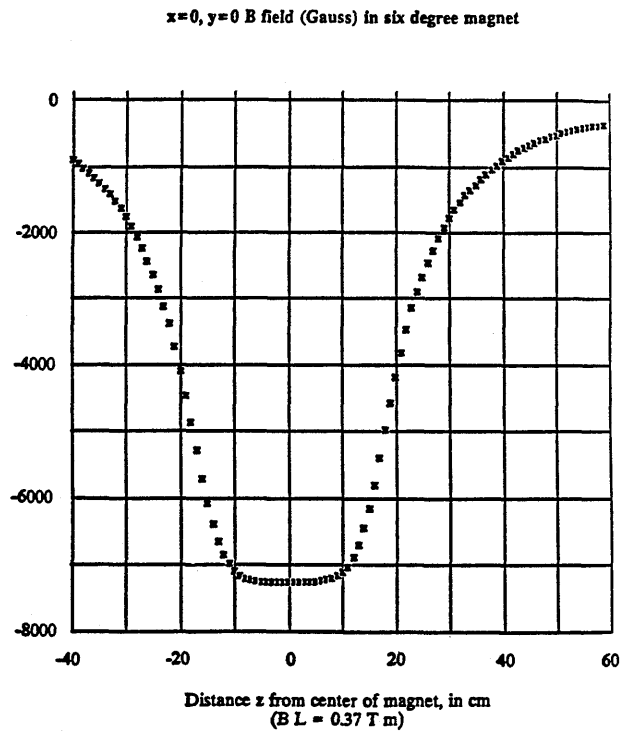

Figure B28. Vertical magnetic field in Gauss in the mid-plane along the beam axis. The field has been calculated with the code Tosca.

Production orders for the magnet components, with the exception of the vacuum vessel, have been let. Delivery is expected in August, 1989. The maximum strength of the rampable magnet field is 0.38 Tesla meters, suitable for bending 500 MeV protons. The maximum field in the center of the gap is 0.75 Tesla. At this field, all iron parts of the magnet are still well below the saturation point.

The entrance of the magnet will be separated from elevated gas pressure in the target area by a very thin mylar entrance aperture with a 2 cm hole. This design has two purposes: a) to suppress any gas flow from the target section into the magnet and beyond; and b) to present no perturbation to the circulating beam. Two 20.3 cm diameter pipes for pumping of the magnet vacuum chamber are provided. It is expected that the vacuum inside the chamber will be below 10^{-8} Torr at all times. Gas loading into the Cooler ring on the downstream side is reduced by connecting the vacuum vessel to a 2.5 cm diameter section of the Cooler beam tube, which is pumped from the downstream side as well.

The magnet vacuum vessel has three removable flanges. The exit for small angles to the left is covered for the $p+p \rightarrow p+n+\pi^+$ experiment by a 13 mg/cm^2 Kevlar foil of vertical aperture 22 cm and horizontal aperture 40 cm, located as close to the exit beam pipe as practical. This foil is thin enough to permit the exit of light ions and protons into the air with minimal ($\pm 0.1°$) scattering. This foil-bearing flange can be replaced by

a bakeable solid steel flange. It can also be replaced by a closed vacuum vessel holding detectors, as long as a good vacuum can be maintained.

A second flange, covering the neutron 0° to 30° direction, is made of thin (0.2 cm) stainless steel and thereby provides minimum interference with the outgoing neutrons, e.g., for the $p+p \rightarrow p+n+\pi^+$ experiment. This flange also is replaceable by other suitable attachments. Finally, a third flange is located on the right side of the beam to permit attachment of detectors for negatively charged pions, such as may be encountered in a $p+d \rightarrow p+p+p+\pi^-$ interaction. All flanges are provided with grooves for Helicoflex seals. These new metal seals are flexible and reusable a number of times. They also need a smaller load than the solid copper seals conventionally used. The magnet vacuum vessel and the target box will be connected by a special adapter.

It is expected that the target, the magnet and the vacuum vessel will be generally available to users of the T-site and will be maintained by IUCF. The major portion of the cost of this equipment has been supported by an NSF grant given to Daehnick, Dytman, and Jacobs as facility users.

B.4.4. Detectors

The kinematically complete determination of the 3-body final state of the $pp \rightarrow pn\pi^+$ reaction requires the detection of 5 degrees of freedom of the outgoing particles. The degrees of freedom measured to highest accuracy are the ϕ and Θ angles for the neutron, the ϕ and Θ angles of the charged particles (pions or protons), and the energy of the charged ejectile. Wire chambers for ray tracing, energy detectors, and a neutron hodoscope have been developed in Pittsburgh. A wire chamber prototype, and portions of the hodoscope, have been tested successfully with beam in the past year.

a) Neutron hodoscope

The neutron hodoscope consists of fourteen 5 cm × 15 cm × 120 cm Pilot F scintillators with one phototube at each end stacked such as to present a cross sectional area of 70 cm × 120 cm. The detector is movable, and will be located at distances of 2.5 to 7.5 m from the target. The scintillators and the support structure for the neutron hodoscope are complete. Position along the bar is measured by the time difference for light transport to the left and right ends of the detectors. Tests of two of the bars with 100 MeV protons have yielded a position resolution of 2.5 cm FWHM. For the closest detector location (2.5 m) this corresponds to a determination of the neutron with an error of 0.3°. The error decreases linearly at larger distances from the target. The vertical resolution is less accurate by a factor of 2, because of the 5 cm height of the detector bars. Instantaneous counting rates of up to 800 kHz have been handled without significant resolution deterioration. The complete neutron hodoscope will be tested during the summer of 1989.

b) The wire chambers

Ray tracing of the charged particles is accomplished by the use of four "horizontal" drift chambers. These chambers measure positions in x and y to about 0.25 mm accuracy. They are separated by 30 cm to measure the ϕ and Θ angles, too. After passing through the chamber array, the outgoing proton passes through an E counter, used for particle identification and timing purposes, and stops in a thick plastic scintillator that serves as an energy detector. The wire chambers are proportional drift counters with a sense wire spacing of 8 mm. The wires are read out with LeCroy 2375 DC preamplifier and

discriminator cards feeding into a LeCroy multiwire CAMAC-based TDC system. These wire chambers cover an area of approximately 22 cm × 45 cm; they have been constructed and bench tested at Pittsburgh. So far, only a shorter prototype drift chamber has been tested at IUCF. With 90 MeV protons as projectiles, resolutions of better than 0.25 mm were obtained. The design of the wire chambers follows that of Pile, et al., at Brookhaven. The negative electrodes are held at −600 V, while the positive sense wires have a potential of +2500 V. For such voltages, amplification is more than adequate; however, at this point, the reliability of the large chambers under prolonged use is still untested. A concentrated effort is under way to match the very satisfactory results obtained with the prototype chamber.

While each component has been tested in-beam and has met or exceeded expectations, the entire apparatus has not yet been used as a unit. Our primary project for summer and fall of 1989 will be to complete and test the final apparatus for the CE03 experiment.

B.5. Measurements in Preparation for Cooler Experiments

A. Berdoz, J.E. Goodwin, H.O. Meyer, M. Minty, P.V. Pancella, R.E. Pollock, T. Rinckel, H. Rohdjess, M.A. Ross, and F. Sperisen

B.5.1. Beams for Experiments

a) Background Studies

In a storage ring the phase space contained within the beam pipe defines the transverse acceptance and the (longitudinal) momentum acceptance. The stored beam encounters some material: this is primarily a localized, internal target, but material distributed around the ring in the form of residual gas must also be taken into account. We suppose that electron cooling is active. We further assume that an RF cavity is available in order to maintain the beam energy against energy loss by passage through the target material. Under these circumstances, the distribution of the stored beam ions in phase space is determined by an equilibrium between the cooling process and heating effects due to the presence of material in the beam, and intra-beam scattering.

The width of the cooled momentum distribution, $\delta p/p$, is typically a few times 10^{-5}. It has been predicted and verified experimentally that material in the beam path has a rather small effect on the momentum distribution. In contrast, the transverse phase space distribution in a light-ion ring is very much determined by the material in the beam. The dominant process is Rutherford scattering which may be treated as multiple or single scattering depending on the number of scatterings during the characteristic damping time of betatron oscillations by cooling (typically of order of 1 s). An example for a transverse distribution is displayed in Fig. B29 which clearly shows that only single scattering is responsible for the distribution near the acceptance limit.

The number N of stored ions decreases exponentially with time for several reasons. The dominant loss process is single scattering by an angle large enough to leave the acceptance. If the scatterer is in a section with dispersion, the excitation of betatron oscillations by changes in momentum are also very important. Other, less important loss mechanisms are: exceeding the momentum acceptance due to δ-ray production, nuclear reactions, and

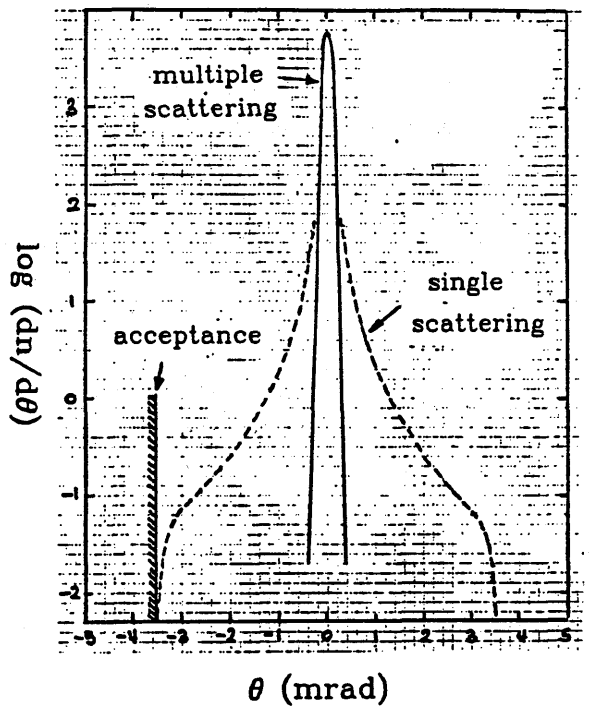

Figure B29. Projected transverse equilibrium distribution calculated for 108 MeV protons and a 10^{14} cm^{-2} thick N target. The cooling time was assumed to be 1 s.

charge state change of the stored ions (the latter becomes important with increasing ion charge and mass and with decreasing energy).

The finite beam lifetime, τ, means that beam ions leave the ring at a rate of (N/τ). These particles may contribute significantly to experimental background. This is made plausible by the following example. Assume $N=10^9$ particles stored in a ring with $f_R=10^6$ Hz encountering a target of thickness $d=10^{14}$ cm^{-2}. The experimental luminosity is then $L=10^{29}$ $cm^{-2}s^{-1}$. Assume further that the lifetime is $\tau=10$ s and that beam lost along 1% of the ring circumference contributes to background. The target thickness relevant for the production of background is given by the range of the particles and is of the order of $d_B=10^{23}$ cm^{-2}. The resulting "background luminosity" is then $L_B=10^{29}$ $cm^{-2}s^{-1}$, i.e., the same as the experimental luminosity!

It is important to realize that the term "background" is only defined with respect to a specific experimental signature. Investigations of background due to beam loss have been conducted with the Indiana Cooler using the CE01 detector setup that is sensitive to particles scattered at small angles ($1° - 20°$). For these studies it was critical to obtain information about the tracks of the detected protons which was provided by two pairs of wire chambers (see sect. B.3.1.). In order to quantify the generation of background we have defined a parameter k which is the probability that a lost beam particle leads to a valid trigger of the data acquisition electronics. In order to determine k one thus has to measure the background rate, the beam lifetime and the stored current. An example of a background-related measurement is shown in Fig. B30. In this experiment the k-factor was determined as a function of the beam lifetime. The variation in lifetime was induced by the excitation of betatron oscillations by applying RF noise to two localized pick-up electrodes in the ring. Two important facts can be seen from Fig. B30, namely, about 0.1%

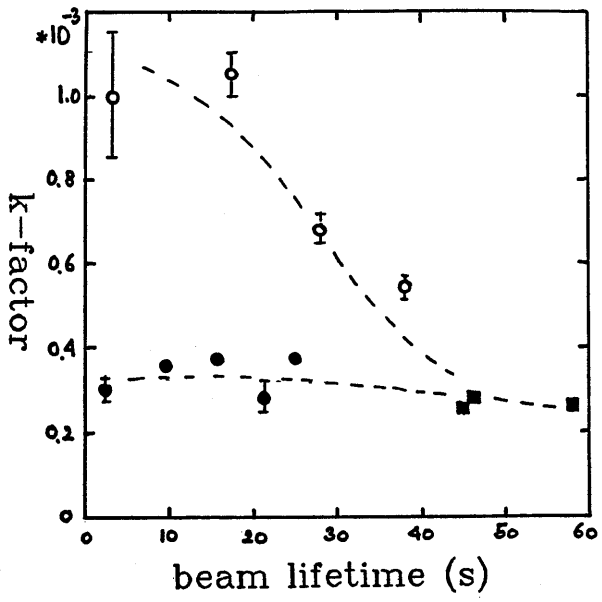

Figure B30. The k-factor (discussed in the text) as a function of the beam lifetime, measured with 148 MeV cooled protons. The lifetime was changed by applying RF noise to a pair of deflector plates, inducing betatron oscillations in the vertical (open circles) and the horizontal direction (closed circles).

of all stored protons convert to valid triggers (a large number) and the k-factor depends on details of the mechanism that leads to beam loss. The latter fact tells us that, as our understanding of the process increases, it will probably be possible to constrain beam losses to sections of the ring where the experiment is not affected.

It is obvious that the question of background is an important criterion in the design of the ring and the internal target which, so far, has been neglected.

b) Aperture-Defining Scrapers

A major part of understanding the generation of background consists in finding the specific locations along the ring circumference where beam ions that have been promoted outside the acceptance actually encounter the beam pipe. This distribution of losses can be controlled. For that purpose, a number of fast-acting, aperture-defining slits are presently under construction at IUCF.

A prototype of a fast acting scraper has been designed and constructed. A side view of the assembly is shown in Fig. B31. Motion of the scraper is accomplished by a magnetic coupling between a solenoid, located outside vacuum, to the moveable scraper which is in vacuum. A current in the solenoid creates a magnetic flux which forces the scraper, the end of which is iron, to the IN position. Extension springs bring the scraper to the OUT position when there is no current. The IN positon is a remotely controlled by a (slowly) movable stop whose position is adjustable to within 10 μm.

The operation of the Cooler requires the the motion of the scrapers to be periodic. They must be outside the ring aperture during injection and, after cooling, must move rapidly into position. The motion will typically be 50 mm in 0.5 s, or less. Initial bench testing of the scrapers in air indicates a lifetime of 10^6 operation cycles without mechanical failure of the assembly. The next stage of testing will be operation of the scaper in vacuum similar to the Cooler vacuum (10^{-9} Torr). A study of the ring parameters is currently underway to decide the best location of the scraper slits.

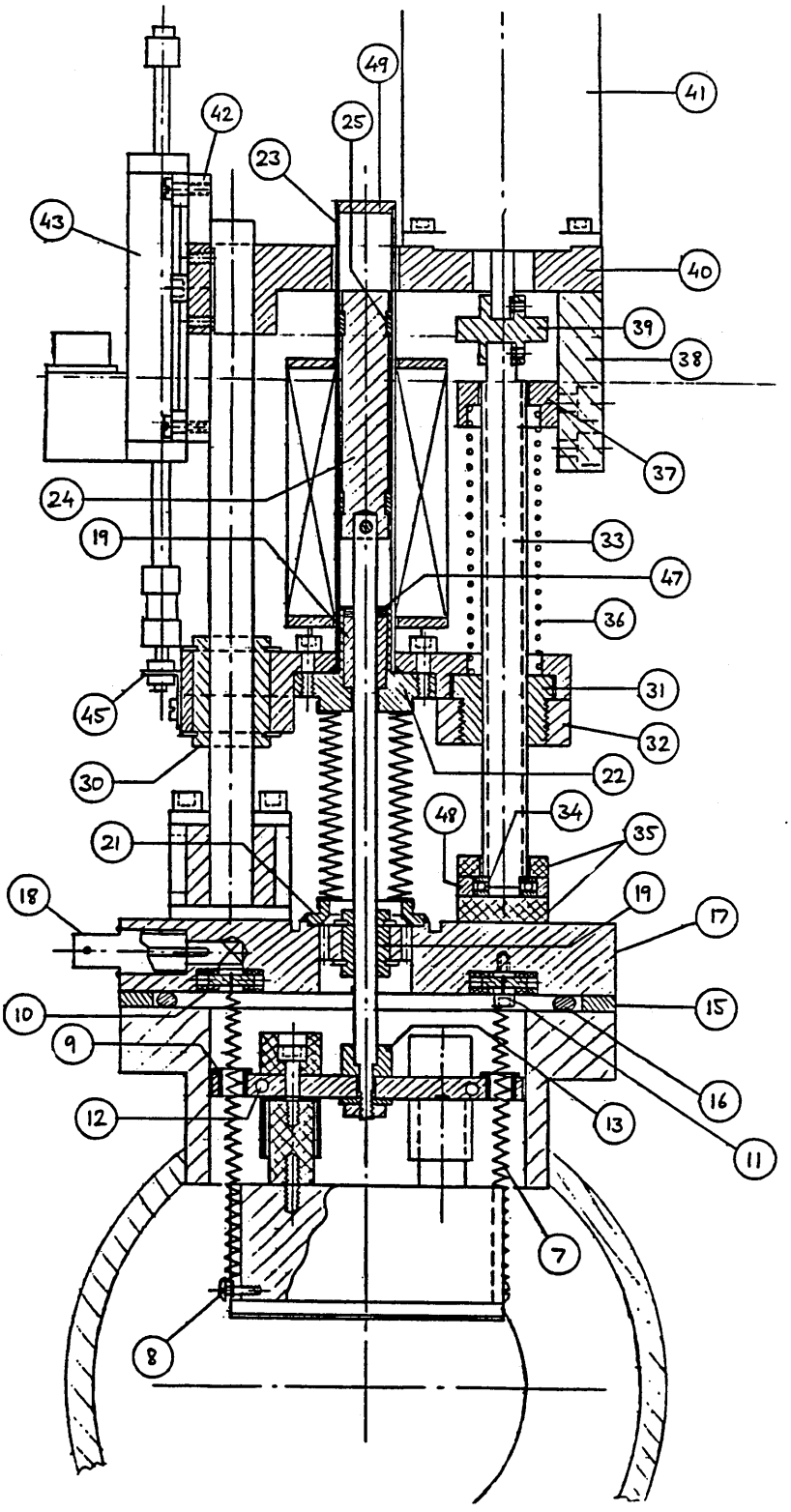

Figure B31. Side view of the assembly an aperture-defining the scraper slit.

B.5.2. Polarization and Cross Section Measurements

According to the Cooler research program, polarized hydrogen beams will play an important role. The key ingredients in providing a stored, polarized beam are stacking injection and stability of the stored polarization. During a recent run we were able, upon first try, to longitudinally stack, store, and cool six turns of polarized, 120 MeV protons (up to 10^5 per fill) and to show that it is possible to compensate for spin precession in the longitudinal field of the cooling solenoid. The beam polarization was measured with a 4.5 mm thick graphite skimmer target and the detector system in the G section. The polarization of the stored beam, measured after a few seconds, was in agreement with the injected beam polarization. Further study is required to investigate the long-term stability of the stored polarization.

The difference between counts with initial polarizations of opposite signs, normalized by their average are shown as a function of the azimuthal angle ϕ in Fig. B32. The expected $\cos\phi$ dependence is clearly visible and can be used to determine the beam polarization. More about polarized beams in the Cooler can be found in the account of experiment CE05, elsewhere in this report.

The task of measuring an absolute cross section is more difficult than the relative measurement needed to determine polarization. Since the gas target with its many parts close to the beam axis has been removed from the G target box, we are able to localize the source of scattered protons (see Fig. B22) using the tracking capability of the wire chambers (see section B.3.2). Thus, events from the target can be cleanly isolated. A determination of the luminosity, however, is difficult for two reasons. First, the measurement of the stored current which is deduced from the signal obtained from a wall gap device depends on the time structure of the beam and includes a component caused by RF noise; an optimistic

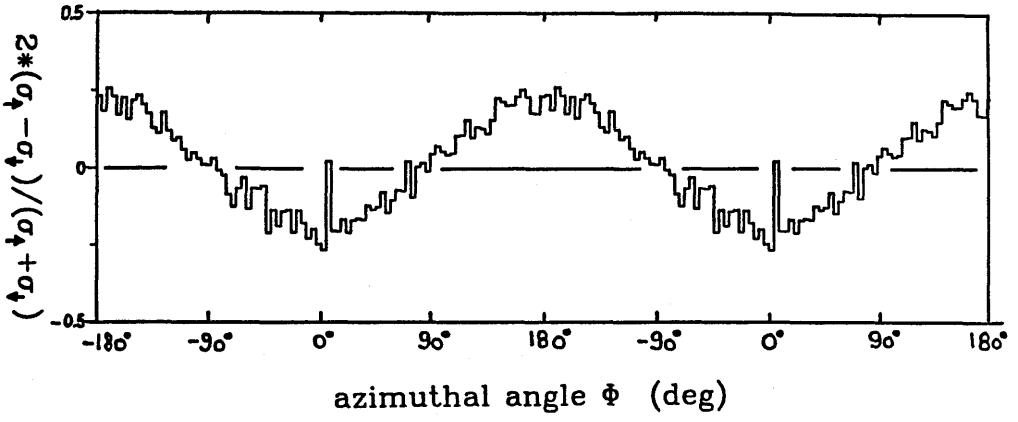

Figure B32. Azimuthal distribution of 120 MeV polarized, stored, cooled protons scattered from a ^{nat}C skimmer target. Shown is the difference between the numbers of events with spin "up" and "down" divided by their average. Scattering angles between 5.5° and 19° are included. A stored beam polarization of 0.77 ± 0.02 was deduced from this particular distribution.

estimate of its uncertainty is 20%. Second, the target thickness is not well known. In the case of a fiber this is due to poorly known fiber dimensions as well as an uncertainy caused by the detailed motion of the fiber relative to beam. In the case of a skimmer target, the effective target thickness depends sensitively on the angle between the skimmer and the beam axis (see section B.2.).

In a series of runs at 108 MeV various target configurations were compared. The detector geometry was set to cover scattering angles between 5° and 17° (for a carbon target, this corresponds to an integrated cross section of about 70 mb). The beam current at the beginning of the cycle was typically a few hundred nA. It was integrated during the run and the total number N of stored protons was deduced. The micro-ribbon used had a linear density of 1.0×10^{15} carbon nuclei per cm. The 'efficiency' (the number of events from the target divided by the number N of stored protons) determined with a fiber moving periodically across the beam was 1.3×10^{-4}; almost the same value was obtained when the beam was moved across the stationary fiber by modulating the RF frequency. Given our knowledge about the beam current and the fiber size and motion, we would have expected about a factor of 2 less. Using a 4.5 mm carbon skimmer target with the beam slowly moved towards the edge of the skimmer, the efficiency was found to be 7.8×10^{-4} which is about a factor of 5 less than expected, assuming that all stored protons eventually go through the target where they see the full thickness (compare section B.2.3.). An interesting test of our understanding of the beam target interaction was a measurement with the fiber stationary and the beam slowly moved towards the fiber (as is done with the skimmer). In this case the efficiency was a few times 10^{-5} with less than 10% of the registered events originating in the fiber. This figure depends on the rate with which the tail is populated by scattering from the residual gas and the effects of the presence of the fiber on the transverse distribution. Attempts to explain the measured value have so far not been successful.

Although qualitative agreement was obtained between the observed number of scattered protons and the expected value, based on the known cross section and our knowledge of the target and beam parameters, it is clear that a reliable luminosity monitor is necessary whenever absolute cross sections are to be determined with the Cooler. This may be a nuclear reaction or an atomic process of known cross section. Then, only a relative angular distribution needs to be measured. This has been demonstrated, as shown in Fig. B33, for elastic scattering of 108 MeV protons from carbon.

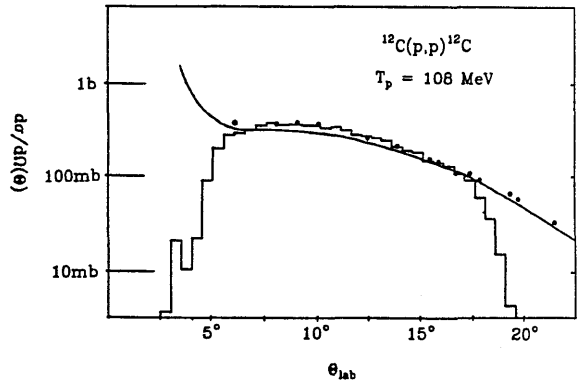

Figure B33. Center-of-mass cross section angular distribution for $^{12}C(p,p)^{12}C$ elastic scattering at 108 MeV versus the lab scattering angle. The histogram represents the Cooler data. The dots are from a conventional experiment with the old IUCF spectrograph at 120 MeV and the curve is an optical model calculation at 120 MeV. The overall normalization of the Cooler data has been adjusted.